Journal of Geophysical Research: Solid Earth

RESEARCH ARTICLE
10.1029/2018JB016165

An Extended Grain-Based Model Accounting for Microstructures in Rock Deformation

Yahui Zhang[1], Louis Ngai Yuen Wong[1], and Ka Kit Chan[1]

[1]Department of Earth Sciences, The University of Hong Kong, Hong Kong

Key Points:
- An extended grain-based model (EGBM) is developed for realistic simulation of crystalline rocks
- Digital image processing (DIP) technique is used for extracting grain boundaries
- Initial microcracks are incorporation by a discrete fracture network (DFN)

Correspondence to:
L. N. Y. Wong,
lnywong@hku.hk

Citation:
Zhang, Y., Wong, L. N. Y., & Chan, K. K. (2019). An extended grain-based model accounting for microstructures in rock deformation. *Journal of Geophysical Research: Solid Earth*, *124*, 125–148. https://doi.org/10.1029/2018JB016165

Received 1 JUN 2018
Accepted 25 NOV 2018
Accepted article online 28 NOV 2018
Published online 5 JAN 2019

Abstract Reliable prediction of the rock fracturing process is a challenging issue in exploitation of deep earth resources in which artificial creation of complex fracture networks is employed. The grain-based modeling (GBM) approach is a promising numerical technique for its unique capability to simulate the fracturing behavior of crystalline rocks. An extended grain-based model is developed to improve the traditional Voronoi GBM from two aspects. First, digital image processing technique is presented to incorporate actual rock microstructures into the numerical model. Second, the effect of initial microcracks is considered by integrating a statistical discrete fracture network model into GBM. By simulating semicircular bending tests on 16 extended GBMs and 3 Voronoi GBMs, the effects of rock microstructures and initial microcracks on microcracking behavior and mechanical properties are analyzed. Cracking patterns are classified into four types for the first time with respect to fracture toughness and crack initiation threshold. The results indicate that the use of a statistical structure or a purely deterministic GBM without consideration of initial microcracks cannot realistically describe grain-scale discontinuities, which likely leads to biased evaluations of the rock failure process.

1. Introduction

Rock fracturing has been one of the most concerned issues in rock engineering practice, such as underground excavation (Tsang et al., 2005), shale gas production (Gandossi, 2013), rock slope stability (Brideau et al., 2009), and enhanced geothermal systems (McClure & Horne, 2014). The overall behavior of the fractured rock formations is mostly accounted for by the effect of fractures associated with the distortion of fractured systems, stress redistributions, evolution of fluid flow channels, etc. Therefore, the interest of understanding the fractured system has been attracted by the geometrical and mechanical representations of the fracture network (Cai & Horii, 1992; Dershowitz & Einstein, 1988). In the cases of ground works where field observation is practically feasible, some measurement techniques such as window and scanline mapping or borehole imaging are commonly used for discontinuity data collection (Prange & LeFranc, 2018; Priest & Hudson, 1981). Field data, however, are generally empirically measured owing to a lot of inherent uncertainties introduced by spatial variations in rock heterogeneity and discontinuity (Hajiabdolmajid & Kaiser, 2003). As a special application, the study of enhanced geothermal systems is highly challenged by a proper evaluation of the hydraulic fracturing response of the geothermal system due to the deep burial (>3,000 m). These difficulties in large-scale field investigation promote the development of small-scale (laboratory scale) tests for understanding the mechanism of rock fracturing.

A large number of laboratory tests have been conducted on both rock materials including marble, granite, limestone, shale, and sandstone (Feng et al., 2009; Morgan et al., 2013; Nezhad et al., 2016; Yang et al., 2013; Zou & Wong, 2014) and rock-like materials (e.g., gypsum; Wong & Einstein, 2009a, 2009b; Zhao et al., 2016). These experimental studies increase our knowledge of the effect of preexisting discontinuities on crack initiation, propagation, and coalescence under external loadings. Preexisting rock discontinuities studied in laboratory specimens can be generalized into two types: inherent discontinuities (stratification, foliation, layering, schistosity, etc.), which lead to anisotropic mechanical behavior, and structural discontinuities (shear zones, fissures, faults, joints, etc.) that induce strain localization. Inherent discontinuities that are formed by alternate depositions are represented by regularly aligned weak planes (Nezhad et al., 2018; Tan et al., 2015). On the other hand, structural discontinuities are usually prefabricated in specimens in the form of single flaws (Wong & Einstein, 2009c; Zou et al., 2016), double flaws (Zhao et al., 2016), or an array of flaws (e.g., en-echelon flaws) (Cheng et al., 2015). Combined influence of the two types of rock discontinuities was also investigated (Morgan & Einstein, 2017). The findings

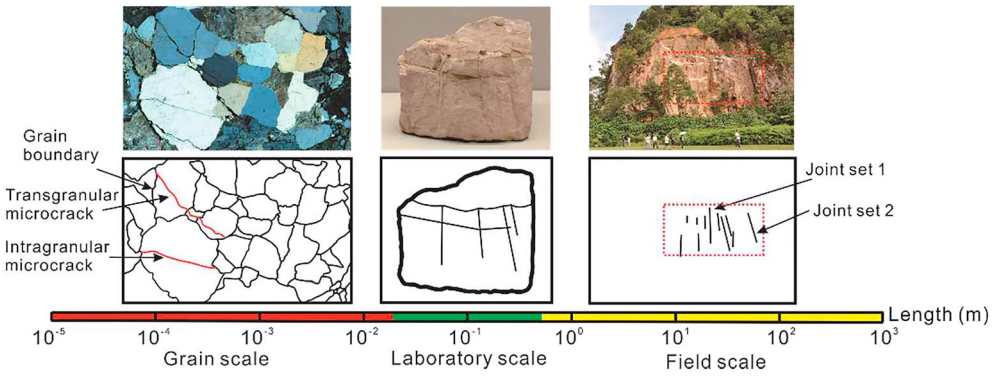

Figure 1. Characterization of rock discontinuities observed at multiscales: field scale (right): a typical jointed rock slope; laboratory scale (middle): a mudstone specimen; and grain scale (left): a thin section image of Hong Kong granite showing distinct grain boundaries and microcracks.

of these studies have contributed to comprehensive conclusions, including classifications of crack types, coalescence patterns, effect of bedding/flaw geometries (e.g., inclinations, bridging angles, and ligament lengths) on crack initiation and coalescence stress, stress-strain behavior, and failure strength of the fractured rock.

Most laboratory studies, which focus on generalization of the correlation between observable discontinuities and rock cracking process, assume that the solid rock matrix is homogeneous and isotropic. This is because the complex nature of rock in terms of its multiscale heterogeneity and discontinuity (see Figure 1) makes the realistic characterization of rock structure difficult. Since macroscopic rock failure is attributed to complicated micromechanisms that are involved in the cracking process (Hajiabdolmajid & Kaiser, 2003), reliable interpretation of the microscopic fracturing mechanism relies on an in-depth knowledge of the effects of grain-scale structures. Chen et al. (2016) found that the introduction of weak bands is insufficient to capture the entire anisotropic mechanical behavior of transversely isotropic shale rocks, while other types of inclusions (e.g., quartz, calcite, and dolomite) forming local heterogeneity should also be considered. Meng and Pan (2007) presented quantitative correlations between mineral compositions and failure duration, microstructures, and failure duration, which indicate significant reliance of macromechanical properties of rocks on their petrographic characteristics.

In face of the major difficulties of observing the internal microstructures and nonrepeatable operation on the same specimen encountered in physical tests, various numerical techniques have also been developed and employed to help model and visualize the microcracking process. In finite element methods, rock heterogeneity is implicitly introduced by decreasing mechanical parameters, such as cohesion coefficient and elastic modulus, in predefined locations to create weak planes that affect fracture geometry and propagation (Dokhani et al., 2016; Liu et al., 2007; Nezhad et al., 2018; Tang et al., 2000; Zeng & Wei, 2017). In contrast, weak layers can be intuitively embodied in the discrete element method (DEM) (Duan & Kwok, 2015; He & Afolagboye, 2017; Park & Min, 2015; Tan et al., 2015; Xu et al., 2018; Yang & Huang, 2014). Although computational demand tends to hinder its large-scale applications, the DEM approach is favorable for its versatility to capture the geometric complexity of rocks at the grain scale. With the hybrid finite-discrete element methods, preexisting microcracks are incorporated by either initial characterization (Hamdi et al., 2015) or reproducing the end effect (Cai, 2013; Lisjak, Grasselli, & Vietor, 2014; Lisjak, Tatone, et al., 2014; Mahabadi, 2012). Zhang and Wong (2018) systematically assessed the capabilities and limitations of a number of numerical methods for simulating rock deformation and failure from a microstructural perspective.

Natural (initial) microcracks observed at the grain scale can be classified into three types, namely, grain boundary cracks, intragranular cracks, and transgranular cracks (Lim et al., 2012). The key role of initial microcracks in dominating the fracturing process has been well recognized as stress concentrators that can lead to local failures (Lajtai, 1998). In the context of numerical simulations, most studies consider only grain boundary microcracks, but less effort has been placed on the characterization of

intragranular and transgranular cracks (Hamdi et al., 2015; Hofmann, Babadagli, Yoon, et al., 2015). For accurate representation of grain-scale heterogeneity and discontinuity, microcomputerized tomography scanning technology and thin section images are employed to obtain microscale phase distribution and microcracks, respectively, which are then directly mapped to a combined finite-discrete element model to simulate the tensile behavior of crystalline rocks (Mahabadi et al., 2014). With similar motivations, we developed an extended grain-based model (extended GBM) based on the discrete element methods in a more low-cost and convenient way. This is crucial for advancing the methodology to a level where it is easily applicable by a large community. The extended GBM is an integration of two well-established models: a GBM and a discrete fracture network (DFN) model. GBM is used to reproduce the microstructure of a real rock based on the results obtained from digital image processing. Meanwhile, the statistical DFN model captures the effect of initial microcracks that is not accounted for in the conventional GBM.

This paper is structured as follows: sections 2 and 3 describe the digital image processing technique and the analysis of thin sections to obtain rock microstructures and statistical properties of microcracks, respectively. Section 4 introduces the extended grain-based modeling approach. Simulation results and discussion are presented in section 5, followed by the conclusions in section 7.

2. Digital Image Processing

2.1. Rock Sample and Image Acquisition

Kowloon granite is chosen as the rock sample to illustrate the processing of images and for subsequent simulations. The rock cores that are made available from a ground investigation project in Hong Kong, China, are intact and fresh. The relatively large grain size and distinct grain structure of Kowloon granite set the convenience for both visual observation and computer analysis. Based on the thin section study, four major kinds of constituent minerals have been identified, namely, alkali feldspar (K-spar), plagioclase (Pi), quartz (Q), and biotite (Bi).

Digital image processing refers to processing of digital images with the use of computer algorithms. Digital image processing in this study is driven by the demand of numerically reproducing the microstructural characteristics of the real rock. A digital image stored in the computer can be of a raster (pixel based) or a vector type. Raster images give continuous tone and soft color blends, while the formation of a vector image is like drawing the outline of the object and filling each part with different colors, thus exhibiting a clear distinction between each color (Sedgewick, 2002). Raster images that can be obtained by handy equipment such as digital cameras are the common image formats (including jpg, png, bmp, and gif) used both on website and for printing. To this end, raster images are taken as the image source in this study, so that the manipulation is based on pixels. Further, the processed raster image will be converted into a vector image for extraction of the fabric information.

The flat specimen surface is first photographed by a digital camera. However, a poor image with faint or obscured features will degrade not only the perceptual quality of the image but also the interpretation of the features (Plataniotis & Venetsanopoulos, 2013). To achieve a more accurate image analysis, the rock surface needs to be pretreated by mechanical grinding to improve the quality of the image. After surface treatment, the specimen is placed on a white paper alongside a scale so that the dimension and orientation of the image can be calibrated.

2.2. Image Segmentation

The purpose of image segmentation is to separate the four minerals based on their color properties. Since the colors of minerals are dictated by their complex chemical compositions and physical structures (Z. Li et al., 2017), each type of mineral appears to be unique in color. However, each of the same mineral grain cannot be digitally characterized by an identical color owing to subtle variations prevailing among individual mineral grains based on the pixel-based interpretation of the image.

The standard RGB space is commonly used for image representation, in which each color is a combination of red, green, and blue in different strengths. Nevertheless, RGB representation is very obscure to human visual perception, thus making it difficult to segment images in the RGB space. Other commonly used color systems including HSI (hue, saturation, intensity) color space (Chen et al., 2004),

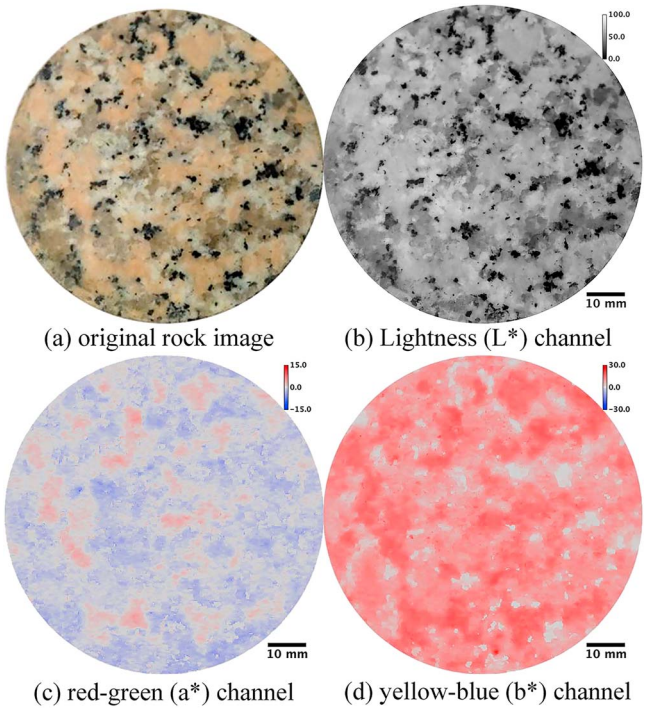

Figure 2. Rock specimen image shown in the three channels of L*a*b* color space.

CMYK (cyan, magenta, yellow, and black) color space (Mark & Billo, 2002), and L*a*b* color space (Z. Li et al., 2017) have been applied to rock physics. In terms of device independence and the wider color gamut, L*a*b* system (L* for lightness and a* and b* for green/red and blue/yellow color-opponent dimensions, respectively) is the most suitable for computer analysis (Tkalcic & Tasic, 2003). Especially, the lightness channel is designed to closely match human perception of lightness. Therefore, RGB images are converted to the L*a*b* color space in the present study.

A rock image is shown in the L*a*b* color space for revealing the contrasts among minerals in each channel (see Figure 2). In the lightness channel, feldspars (K-feldspar and plagioclase), quartz, and biotite show quite different strengths, where biotite is the darkest (lowest value) and feldspars are the lightest (highest value). An imperceptible difference has been observed between the two feldspars in L* channel. Nevertheless, K-feldspar and plagioclase are separable in blue-yellow (b*) channel (see Figure 2d), in which K-feldspar has a higher value (i.e., more yellow component) due to its pinkish nature. Therefore, lightness value is used for separating biotite, quartz, and feldspars, and b* channel is then applied to differentiate plagioclase and K-feldspar.

Histograms of L* and b* channels are generated for selecting thresholds to quantitatively characterize each mineral, as shown in Figure 3. The range of L* channel is between 0 (dark) to 100 (light), in which two peaks are observed. The darker and the lighter peaks respectively correspond to biotite and feldspars. Quartz appears to be in the middle because of its semitransparent nature. The only peak shown in b* channel can be applied to tell K-feldspar apart from others. Table 1 provides the thresholds used for the segmentation of four rock images. Figure 5b shows the results of image segmentation. Table 1 reveals the thresholds are not exactly the same for different rock specimens due to the variations in the mineral colors, light conditions during photographing, etc.

2.3. Image Enhancement

A number of factors, such as noise introduced during photographing, variations in mineral colors, and uneven surface of the rock specimen, can contribute to appearance of unwanted features (e.g., stray dots) in the segmented image. Image enhancement is hence performed to appropriately simplify the grain structure to facilitate the subsequent modeling. Because the complexity of uncertainties makes manual correction impractical, image enhancement is generally achieved by applying computation algorithms. Some fairly simple yet powerful image enhancement methods have been formulated, such as the averaging method and low-pass filtering method. All these methods may blur the edges and other sharp details. Comparatively, the median filter method can protect the edges of different parts by replacing the value of a pixel in images with the median value of its neighboring pixels. Therefore, median filter is selected to enhance the segmented image (Gonzalez & Woods, 2012).

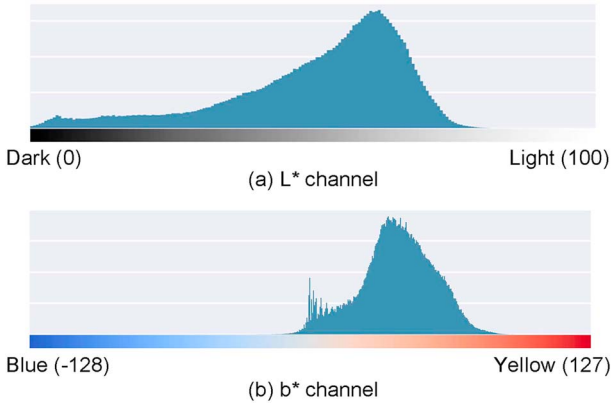

Figure 3. Histograms of a L* and b b* channels for separating minerals.

Figure 4 illustrates the principle of the median filter. For every pixel, its neighboring pixels (bordered by the red dotted rectangle) and the pixel itself are considered. The median kernel is a (2*size+1) times (2*size+1) square, where size is referred to as filter radius (1 pixel in Figure 4). The median value, which is defined as the middle value of the window data in sorted order, will then replace the original value of the pixel. Therefore, filter radius is a critical parameter in the median filter method in controlling the *smoothness* of the output image. Selection of the filter radius is a trial-and-error process depending on image resolution and grain size of the specimen. The value is assumed reasonable as the

Table 1
Thresholds Used for Image Segmentation

	Lightness channel (L*)		Blue-yellow channel (b*)
Specimen	Biotite-quartz	Quartz-feldspars	Others-K-feldspar
1	28	55	10.5
2	27	50	11.5
3	27	58	12.0
4	28	60	10.5

generated image preserves the principal features of the specimen. The radius chosen for filtering in this study is 5 pixels.

For the sake of simulation efficiency, tiny grains presented like *specks* are also removed to reduce the complexity of the structure, by replacing the color with that of their surrounding grains. In the rare case that the tiny grain is found in the rim of different mineral grains, the mode type of the tiny grain is determined by the *dominant mineral*, which occupies the highest number of pixels in the vicinity. The enhanced images are shown in Figure 5c. Since the color raster image consists of several color components that decrease computational efficiency, the enhanced color image is then converted to a grayscale image so that each color is dedicated by only one gray-level value.

2.4. Image Vectorization

Based on pixel-by-pixel interpretation, raster images do not explicitly specify the outlines. In order to extract rock fabric, the enhanced images are vectorized using the software Potrace in Inkscape (http://potrace.sourceforge.net). Potrace employs a polygon-based algorithm that works on binary (black-and-white) images to produce a vector outline of the object (Selinger, 2003). For the grayscale image registered by several gray values, each color is separately traced. To reduce the complexity of the vectorized output, the *Optimize paths* method is applied whereby multiple consecutive segments are merged into a single segment. This step, which is at the expense of losing some details, should be carefully performed to produce neither too rounded nor too jaggy outlines. The extracted outlines will serve as the grain boundary fabric (as shown in Figure 5d).

3. Characterization of Microcracks

3.1. Discrete Fracture Network

Direct mapping of discontinuities is difficult because discontinuities generally distribute in rock masses randomly or in sets with complex geometric characteristics. A simplified representation of the fractured system can be realized in the DFN approach. Within the DFN concept, an intact, mechanically homogeneous system is discretized by the insertion of multiple sets of fractures whose geometric properties (e.g., locations, sizes, orientations) within a structural domain are defined by probability distributions (Xu & Dowd, 2010). For the purpose of statistical analysis to derive the probability functions, some systematic measurement techniques such as scanlines or window mapping of outcrops (Priest & Hudson, 1981) have been developed for data collection.

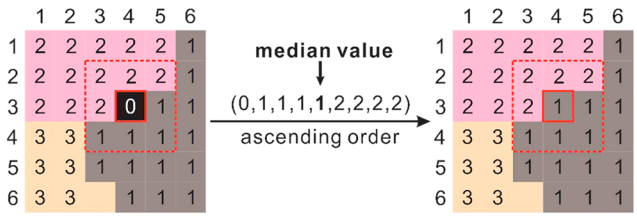

Figure 4. Illustration of removal of stray dots by applying median filter. Filter radius is set as 1 pixel, so each pixel and its eight neighboring pixels are considered for determination of the median value.

At the laboratory scale, a similar concept has been introduced to establish a micromodel (Hamdi et al., 2015; Lisjak, Tatone, et al., 2014) for characterizing initial microcracks. Unlike grain boundaries that can be identified by the chromatic and mineralogical characteristics, deterministic characterization of initial microcracks is practically unrealistic. Inspired by the simulation of large-scale rock masses, initial microcracks are modeled in a statistical way, which aims at incorporating the effect of microcrack heterogeneity that has not been accounted for in the conventional Voronoi GBM.

In line with the generation of the microdiscrete fracture network (μDFN) model (Hamdi et al., 2015), thin sections are analyzed for obtaining the two-dimensional microcrack statistics. Assuming that natural microcracks

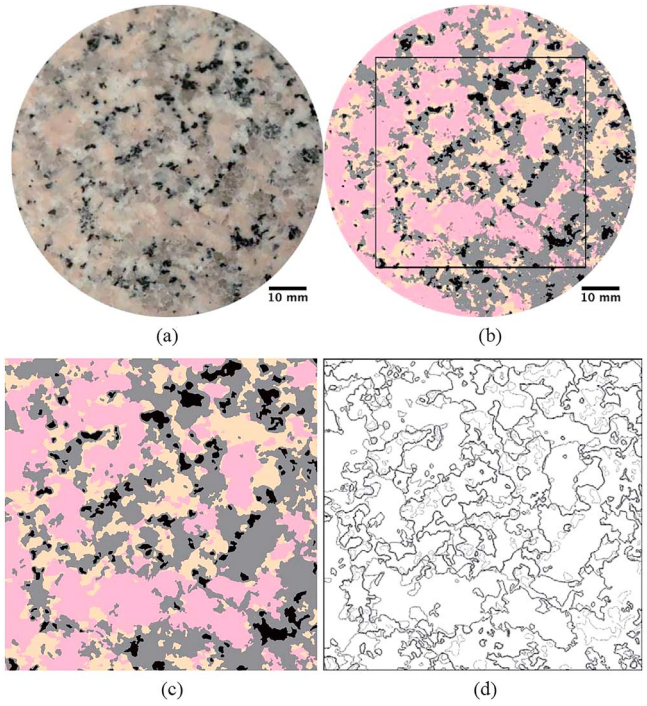

Figure 5. Illustration of image processing: (a) the original image of rock specimen, (b) the segmented image showing mineralogical compositions (pink, light yellow, dark gray, and black represent K-feldspar, plagioclase, quartz, and biotite, respectively), (c) a zoomed-in view of the enhanced image enclosed in (b). Some stray dots and tiny grains are removed by replacing the colors with their surrounding colors and (d) the rock fabric vectorized from (c).

formed within the same mineral type of a rock specimen will have similar properties such as the preferential orientations, microcracks distributed within different mineral types are identified separately. The geometric properties, which serve as input parameters for the DFN model generation, include microcrack size, orientation, and density (P21). Microcrack density is defined as the total microcrack length per unit area. The size and orientation are analyzed using the basic statistical methods such as histogram to identify the best fit probability distribution functions. Different sets of DFN models can be generated and then separately installed into different mineral regions. The presence of microcracks with associated strength degradation is mimicked by weakening the strengths (tensile strength and cohesion) of parallel bonds that cut across the installed DFN.

3.2. Data Collection and Analysis

Two thin section images are analyzed in this study, each of which is stitched together from 58 smaller images of different portions of the examined area. In order to identify the spatial distributions of the microcracks with respect to mineral type, minerals in the thin sections are first manually traced based on the observations under a petrological microscope. The image region is then classified into K-feldspar, plagioclase, biotite, and quartz. Since accurate measurement of individual microcracks is difficult, five principles of microcrack tracing are developed and followed (described in Appendix A1.).

In total, 1,110 micocracks have been manually traced on the two thin section images. Table 2 records the distributions of microcracks within different minerals. Most of the microcracks are found in quartz, while a small portion of microcracks exist in biotite. Very few microcracks are observed in feldspars. Figure 6 provides a portion of the thin section image showing the distribution of microcracks. Hence, only the microcracks within quartz grains are taken into account.

The microcrack properties used to generate a DFN model include length, orientation, and density (P21). Microcrack density (P21) is defined as the total length of microcracks per unit area (Hamdi et al., 2015). The total microcrack length can be calculated simply by summating the lengths of all the microcracks traced within each type of mineral. The total area equals the pixel number, which the mineral occupies multiplied by the unit size of pixel. Then, the equation for microcrack density can be expressed as

$$\mathrm{P21} = \frac{L}{A} = \frac{\sum_{i=1}^{N} L_i}{a \cdot N^{\mathrm{pix}}} \tag{1}$$

where L and A are the total microcrack length and the mineral area, respectively. L_i is the length of ith microcrack, a is the unit size of pixel, and N and N^{pix} are the number of microcracks within each type of mineral and the number of pixels that mineral grains occupy, respectively.

The total length of microcracks (L) traced in quartz area is 379.71 mm, and the total area (A) of quartz is about 249.11 mm^2. By applying equation (1), the microcrack density (P21) is calculated as 1.52 mm^{-1}.

Table 2
Distributions of Microcracks in Examined Thin Sections

Mineral	Total number of microcracks	Percentage
Quartz	1,050	94.59%
K-feldspar	10	0.90%
Plagioclase	8	0.72%
Biotite	42	3.78%

In determination of orientation and length distributions, histograms and probability plots are generated to derive their distribution functions. It can be observed from Figure 7a that the length distribution of microcracks in quartz is well fitted by a lognormal probability distribution function (PDF):

$$P(x) = \frac{e^{\frac{-(\ln x-\mu)^2}{2\sigma^2}}}{\sqrt{2\pi}\cdot x\cdot\sigma} \tag{2}$$

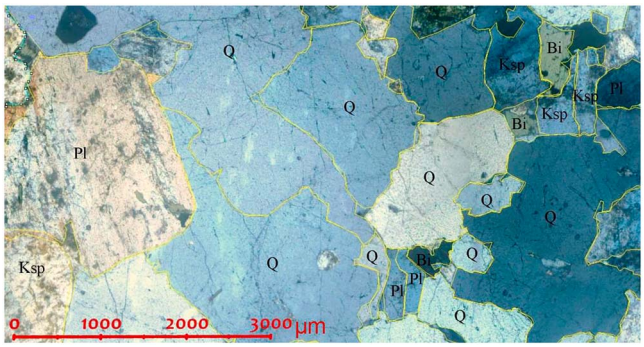

Figure 6. A microscopic image of a thin section in crossed polars (XPL) with identified mineral grains. Q = quartz, Ksp = K-feldspar, Pl = plagioclase, and Bi = biotite.

where x is the microcrack length and μ and σ are the mean and the standard deviation of the distribution, respectively. The fitted values of μ and σ for the PDF of length of microcracks in quartz are −8.13 and 0.65, respectively.

The orientation of microcracks in quartz generally follows the Gaussian distribution (normal distribution), as described by equation (3)

$$P(x) = \frac{e^{\frac{-(x-\mu)^2}{2\sigma^2}}}{\sigma\sqrt{2\pi}} \tag{3}$$

where x is the microcrack orientation ranging from 0° to 180° (exclusive) and μ and σ are the mean and the standard deviation of the distribution, respectively. The values of μ and σ for the PDF of orientation of microcracks in quartz are 96.37 and 41.87, respectively.

4. Numerical Methodology

4.1. Fundamentals of Voronoi Grain-Based Model

Prior to the development of GBM, the DEM-based bonded-particle model (BPM) had been widely used to simulate the mechanical behavior of rock/rock-like materials, (Hazzard et al., 2000; Potyondy & Cundall, 2004; Zhang & Wong, 2014). BPM is based on the assumption that the material consists of discrete particles bonded or cemented at their contacts, and the failure of a contact bond denotes the formation of a crack. Emergent behavior of the material is governed by interaction laws between entities rather than any predefined constitutive relations. Although the BPM approach offers unique advantages for explicitly simulating the entire cracking process, it suffers limitations in terms of capturing the effect of grain interlocking, such as nonlinearity of stress-strain response and a low ratio of tensile to compressive strength (Zhang & Wong, 2018).

The GBM was first introduced into the Particle Flow Code in two dimension (PFC2D) by Potyondy (2010). Compared with BPM, GBM-PFC2D is robust to mimic breakable, polygonal grains in such a way that the original parallel bonds among particles located near grain boundaries are replaced by smooth joint contacts to allow particles sliding along grain interfaces. The mechanical formulation of GBM-PFC2D is graphically illustrated in Figure 8. Details about the description of the parallel bond and the smooth joint contact are given in Potyondy (2010). GBM-PFC2D has been shown to be able to simulate (1) sufficient degree of grain interlocking associated with a reasonable ratio of tensile to compressive strength, (2) nonlinear stress-stain behavior, and (3) the breakage of rock grains to relieve stress localization.

However, a key issue of the GBM approach that has not been thoroughly discussed yet is that the rock fabric employs a Voronoi tessellated structure (referred to as Voronoi GBM hereafter) rather than a real one. Although Voronoi algorithm is robust in its potential to take the polycrystalline morphology into a computational form (Lewis & Geltmacher, 2006), the tessellation process in Voronoi GBM approach considers only first-order properties of the real morphologies: grain size distribution and the number of first neighbors (Quey

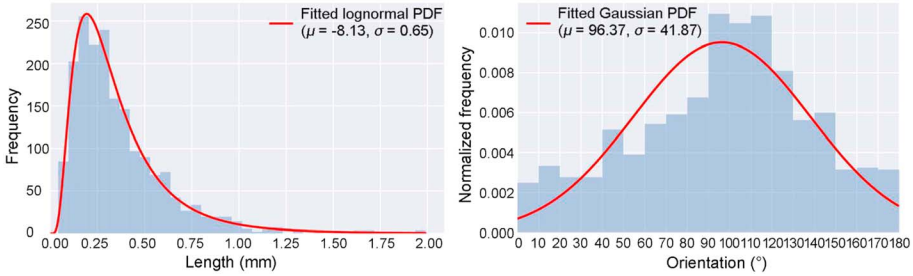

Figure 7. Distributions of length (left) and orientation (right) of microcracks in quartz.

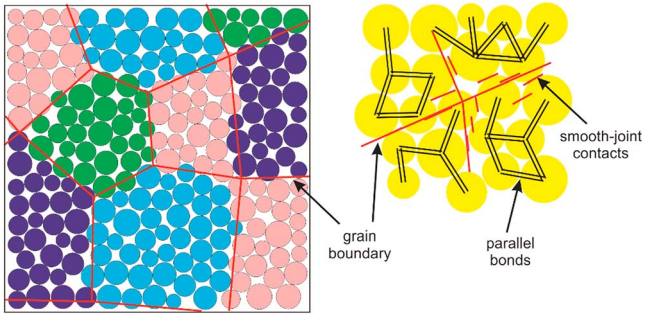

Figure 8. Illustration of mechanical formulation of GBM-PFC2D. Particles in different colors denote different mineral types.

et al., 2011). Other textural characteristics, such as the bounds of minerals and the preferred orientations of crystals, are not acknowledged in the conventional Voronoi GBM. This in some cases leads to errors in representing the realistic 2-D microstructures and anomalous grain shapes that are important in controlling the mechanical performance.

4.2. Generation of Extended Grain-Based Model

The proposed extended GBM follows the same mechanical representation of rock in GBM-PFC2D, in which intragranular contacts and grain boundary properties are simulated by parallel bond and smooth joint contact, respectively. The difference is that rock structure is directly mapped from a real rock specimen rather than employing a Voronoi tessellation. Referring to the principles of the GBM-PFC2D (Potyondy, 2010), extended GBM generation generally follows four steps:

Step 1 - Build an unbonded base material according to the geometry and dimension of the numerical model. Creation of a base model includes compacting initial assembly, installation of specified isotropic stress, and elimination of floating particles. Detailed descriptions of the material genesis procedure can be found in Potyondy and Cundall (2004).

Step 2 - Import the grayscale image into the unbonded model for particle classification. The center of each particle is projected to a pixel in the image associated with a gray value that characterizes the mineral type. This step may introduce slight changes to the grain shape due to the random arrangement of particles and limited resolution of the model. After identification and labeling of particles, different grain properties (parallel bonds) with respect to the mineral type can be assigned.

Step 3 - Import the rock fabric to install grain boundaries by substituting the smooth joint contacts for the original parallel bonds. The orientation of the grain interface is accordingly modified to be that of the grain boundary in the vectorized image. Selection of parallel bond and smooth joint contact parameters will be illustrated in the following subsection.

Step 4 - Generate a DFN model representing the microcrack network. The predictive DFN model is based on probability distributions of length, orientation, and density of microcracks derived from the earlier thin section analysis. Since only the microcracks in quartz grains are considered, the DFN is applied to the quartz region. The parallel bonds (tensile strength and cohesion) that cut across the microcracks are weakened by multiplying a weakening factor ($\alpha_m < 1$) to mimic the effect of strength degradation. The workflow for extended GBM generation is shown in Figure 9.

5. Results and Discussion

5.1. Laboratory Results and Model Calibration

Because the input microparameters for generation of a particle flow code model cannot be mapped directly from the macroscopic material parameters, a set of representative microparameters has to be selected to reproduce the material. This is usually achieved by matching the macroscopic responses of the numerical model via testing with those observed in laboratory tests, such as the uniaxial compressive strength, tensile strength, Young's modulus, and the macroscopic failure pattern (Cho et al., 2007; Potyondy & Cundall, 2004; Yoon, 2007; Zhang & Wong, 2014). Uniaxial compressive test and semicircular bending test are conducted in laboratory for the present model calibration. The calibrated model is simulated under semicircular bending testing to investigate the microcracking behavior and mechanical properties.

For the uniaxial compressive test, the experimental specimen and the 2-D numerical counterpart are prepared in the same dimensions (100 mm in height, 50 mm in length, and 25 mm in width for the laboratory one). However, a smaller numerical model is used in the semicircular bending test to reduce computation time in the subsequent simulations. Previous studies suggest that reducing model size has no significant influence on the results but significantly improves the computing efficiency (Hofmann, Babadagli, & Zimmermann, 2015; J. Li, et al., 2017; Liu et al., 2018; Peng et al., 2017). Considering that each mineral should comprise several particles to allow the breakage of intragranular

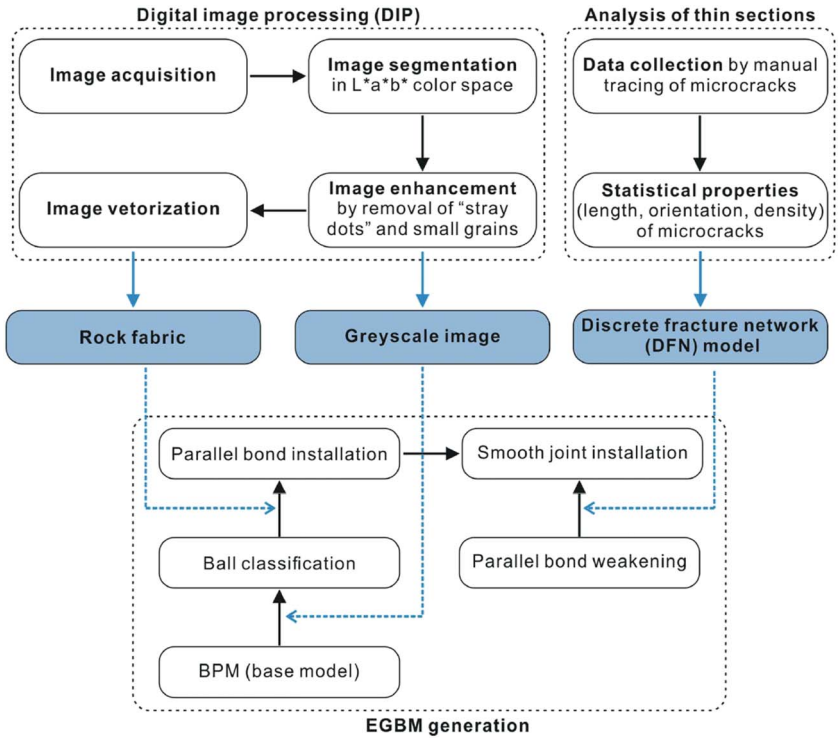

Figure 9. Workflow for extended GBM generation.

contacts, particle radius is set as a uniform distribution between 0.09 and 0.18 mm. The semicircular model includes 20,265 particles. The specimen geometry and the loading arrangement follow the suggested semicircular bending testing method (International Society for Rock Mechanics, 2007), as sketched in Figure 10. Table 3 gives the recommended, numerical, and experimental geometric dimensions of the semicircular bend specimens.

Mode I fracture toughness K_{IC} of the tested semicircular bend specimen is calculated using the equation below (Kuruppu et al., 2014):

$$K_{IC} = Y' \frac{P_{max}\sqrt{\pi a}}{2RB} \tag{4}$$

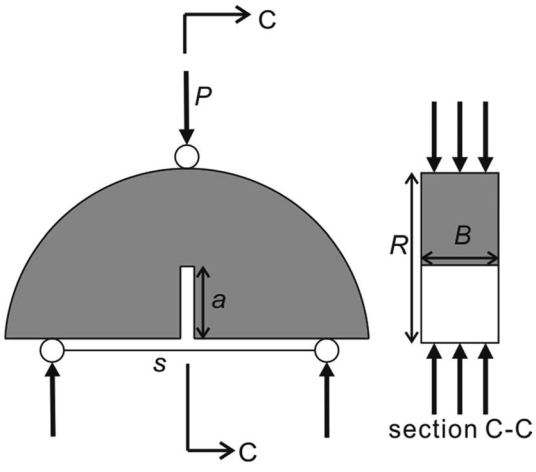

Figure 10. Schematic illustration of semicircular bend specimen geometry and loading arrangement (after Kuruppu et al., 2014). *R* and *B* are radius and thickness of the specimen, respectively; *a* is the notch length; *s* is the distance between the two supporting cylindrical rollers; and *P* is the monotonically increasing compressive load applied at the central loading roller.

where P_{max} is the maximum load applied to the specimen and Y' is the nondimensional stress intensity factor calculated by the formula

$$Y' = -1.297 + 9.516\left(\frac{s}{2R}\right) - \left(0.47 + 16.457\left(\frac{s}{2R}\right)\right)\beta + \left(1.071 + 34.401\left(\frac{s}{2R}\right)\right)\beta^2 \tag{5}$$

in which $\beta = a/R$.

Since numerous microparameters are involved in GBM, selection of these microparameters substantially makes reference to the literature (Hofmann, Babadagli, & Zimmermann, 2015), in which the simulated rocks have almost the same mineralogical compositions as the Kowloon granite. Then, the microparameters are adjusted in a trial-and-error way to match the uniaxial compressive strength and Young's modulus via uniaxial compressive testing, and fracture toughness and macroscopic cracking pattern by semicircular bending test. Notably, microproperties (particle and parallel bond properties) of each mineral are compared with their respective macroscopic elastic parameters in the literature (Hofmann, Babadagli, &

Table 3
Recommended, Numerical, and Experimental Geometrical Dimensions of Semicircular Bend Specimens

Geometric parameter	Recommended value or range[a]	Numerical value	Experimental value
Diameter (D)	Larger of 10 × grain size or 76 mm	50 mm	84 mm
Thickness (B)	Larger of 0.4D or 30 mm	1 m[b]	33.6 mm
Crack length (a)	$0.4 \leq a/R\ (=\beta) \leq 0.6$	12.5 mm	21 mm
Span length (s)	$0.5 \leq s/2R \leq 0.8$	30 mm	50 mm

[a]From Kuruppu et al. (2014). [b]The thickness of a PFC2D model is 1 unit (meter by default).

Zimmermann, 2015). This comparison provides great insights into modifying microparameters with respect to mineralogy. Major adjustment of microparameters to match the uniaxial compressive strength, Young's modulus, and fracture toughness with laboratory data follows the procedure proposed by Bahrani et al. (2014). Based on the results of a sensitive analysis regarding how the mineral and mineral boundary microproperties control the amount and type of microcracks (Hofmann, Babadagli, Yoon, et al., 2015), careful adjustment is further performed to approach the cracking pattern observed in the laboratory test by scanning electron microscope. Several internal loops may be necessary to converge to both the macromechanical parameters and the macroscopic observation. The calibrated microparameters are summarized and further interpreted in Appendix A2.

Figure 11 shows the close match of stress-strain curves regarding the uniaxial compressive strength and Young's modulus. In semicircular bending test, the maximum load (P_{max}) obtained in laboratory is 3.1 kN. By substituting P_{max} = 3.1 kN into equation (4), Mode I fracture toughness (K_{IC}) of the real specimen is calculated as 1.279 MPa·m$^{0.5}$. Using the same value of K_{IC}, the maximum load of the numerical model is about 71 kN (refer to section 6.1 for further interpretation on the mismatch of P_{max} between the numerical and experimental data). Figure 12 shows a comparison of the representative stress-strain curves and macroscopic cracking patterns under semicircular bending test obtained in laboratory and numerical simulation.

5.2. Influence of Rock Fabric on Microcracking Behavior and Fracture Toughness

Sixteen extended GBMs are prepared and tested. Another three Voronoi GBMs are also generated for comparison. The microparameters of Voronoi GBMs are assigned the same as those of the extended GBM. The only difference is that the rock structure in Voronoi GBM is tessellated using the Voronoi logic by matching the grain size distribution with that of a real rock which is obtained from the thin section study. The input parameters for the generation of the three Voronoi structures are given in Appendix A3. Figure 13 compares the microstructure of an extended GBM, which is directly mapped from a real rock specimen with that of the Voronoi GBM.

To compare the microcracking behavior of rocks possessing different microstructures, zoomed-in views of the spatial distribution of microcracks are shown in Figure 14. Because all of the models are consistently shaped and tested under the same conditions, great variations of the main fracture regarding the length, width, and geometry imply that rock microstructures exert a significant influence on rock fracturing behavior. Figure 15 provides the information regarding how different types of microcracks contribute to the fracturing of GBMs. Since smooth-joint contact allows the two adjacent particles to slide and pass through without moving around each other to mimic a weak, smooth interface, shear deformation is easy to accommodate along grain boundaries. As a result, shear and tensile cracks contribute equally to intergranular failure, while the intragranular cracks are dominated by tensile mode (in red).

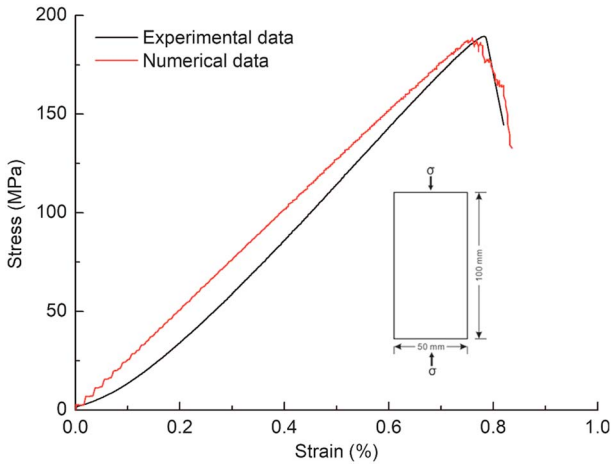

Figure 11. Calibrated stress-strain curve under uniaxial compressive test.

As shown in Figure 15, very few intragranular shear cracks develop in both extended GBMs and Voronoi GBMs. Intergranular microcracks are dominant in Voronoi GBMs, which is in good agreement with the numerical results presented by Peng et al. (2017). Zang et al. (2000) performed uniaxial compression tests on Aue granite specimens to investigate the fracture process zone. In an attempt to induce a discrete shear rupture in the cylindrical specimen, the steel loading plate covered only 80% of the top surface of the specimen. However, the laboratory results measured from acoustic emissions indicate that more intragranular microcracks develop in the rock. Such phenomenon is well captured by the extended GBMs. This is likely to be explained by

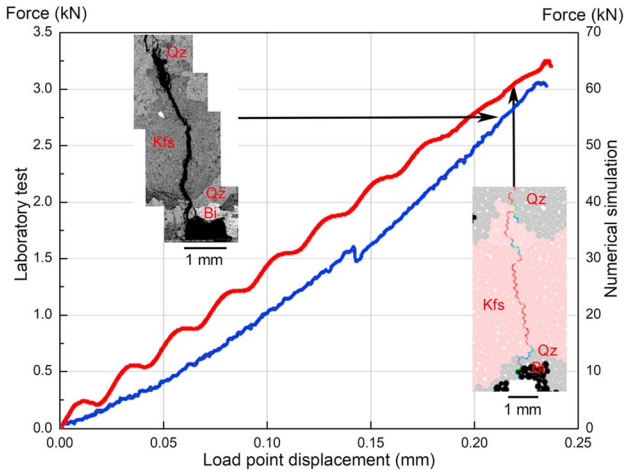

Figure 12. Loading-displacement relationship and macroscopic cracking pattern obtained from laboratory semicircular bending test and numerical simulation. Kfs, Bi, and Qz denote K-feldspar, biotite, and quartz, respectively.

intuitive comparison of microstructures of Voronoi GBMs and extended GBMs (in Figure 13), which suggests that the effect of clustering is underestimated in Voronoi GBMs; that is, the role of intergranular cracking is overestimated. In terms of crack orientation, intragranular microcracks are primarily aligned vertically or subvertically, and the intergranular microcracks are randomly oriented depending on the local orientation of grain interfaces, thus generating a smooth fracture trajectory within the grain and a curved outline along the grain boundary. Therefore, the effect of grain boundary discontinuities can be assessed by the tortuosity of the crack. For this reason, the path of the macrofracture obtained from extended GBM shows a more noticeable tortuous nature as compared with that observed in Voronoi GBM.

It should be noted that in conventional unconfined/confined compressive tests and Brazilian tensile tests where intact specimens without obvious structural defects are used, the stress within the specimen is relatively homogeneous. Multiple microcracks may initiate from different positions and then propagate and coalesce to form the main crack(s). Therefore, the failure pattern is usually characterized by parallel-aligned small cracks. With a manually created notch in the semicircular specimen, crack initiation and propagation are oriented by the highly concentrated stress at the notch tip. The crack will extend from the tip and generally will propagate upward with the traction of localized stress at the crack tip. Comparatively, the areas of the specimen away from the main crack are in a low stress state, cracks are thus less likely to appear (as shown in Figure 14).

To visualize the spatial evolution of the vertical (*y* component) stress, three columns of measurement circles are arranged from the notch tip to the top of the specimen, as shown in Figure 16. The stress within the measurement region is averagely measured owing to the discrete nature of the medium. Therefore, all of the measurement circles are set sufficiently small (1.25 mm in diameter) to show the continuous evolution of the stress in the monitored areas. In all models, the maximum tensile stress always appears at the crack tip, which is responsible for crack extension. Another two sets of measurement circles are also vertically aligned from the supporting points for comparison. Imperceptible is the loading effect as the measurement circles along the two sides are comparable.

From the perspective of macromechanical properties, overestimation of the number of grain boundary cracks in Voronoi GBM is likely to result in a lower peak loading with associated fracture toughness because grain boundary failure is generally easier than grain breakage. In order to validate this speculation, the values of the fracture toughness for all the numerical specimens are calculated using equation (4), and the results are presented in Figure 17. The measured fracture toughness of the 16 extended GBMs varies from 0.75 to 1.43 MPa·m$^{0.5}$, while the values of the three Voronoi GBMs are close but lower, that is, 0.73, 0.78, 0.81 MPa·m$^{0.5}$, respectively. The considerable discrepancy in the results implies that the deterministic contribution of microstructures to the fracturing resistance is significant.

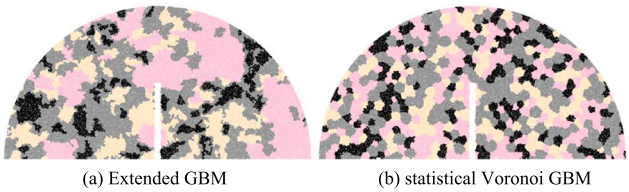

Figure 13. Comparison of rock structures by (a) direct mapping from the real specimen and (b) reproducing statistical properties. Voronoi polygons are convex, equiaxed in shape, and uniform in size. Real mineral grains can be either concave or convex and present great variations in shape.

5.3. Influence of Initial Microcracks on Microcracking Behavior

In order to embody the role of initial microcracks in rock fracturing, microcracks after specimen failure are depicted as bicolored lines (see Figure 18), in which green represents those coinciding with the initial microcracks installed by the DFN model. No green microcracks are spotted in EGBM-6, EGBM-8, EGBM-9, EGBM-11, EGBM-13, and EGBM-16, because the main fracture detours from the quartz region or propagates along the boundary of quartz. In the remaining extended GBMs, about 30.7% of the total intragranular microcracks in quartz form in the weakened bonds. To further investigate the deterministic contribution of initial microcracks to microcracking behavior, EGBMs-1, EGBMs-2, EGBMs-3, EGBMs-4, EGBMs-5, EGBMs-7, EGBMs-10, EGBMs-12, EGBMs-14, and EGBMs-15 are retested

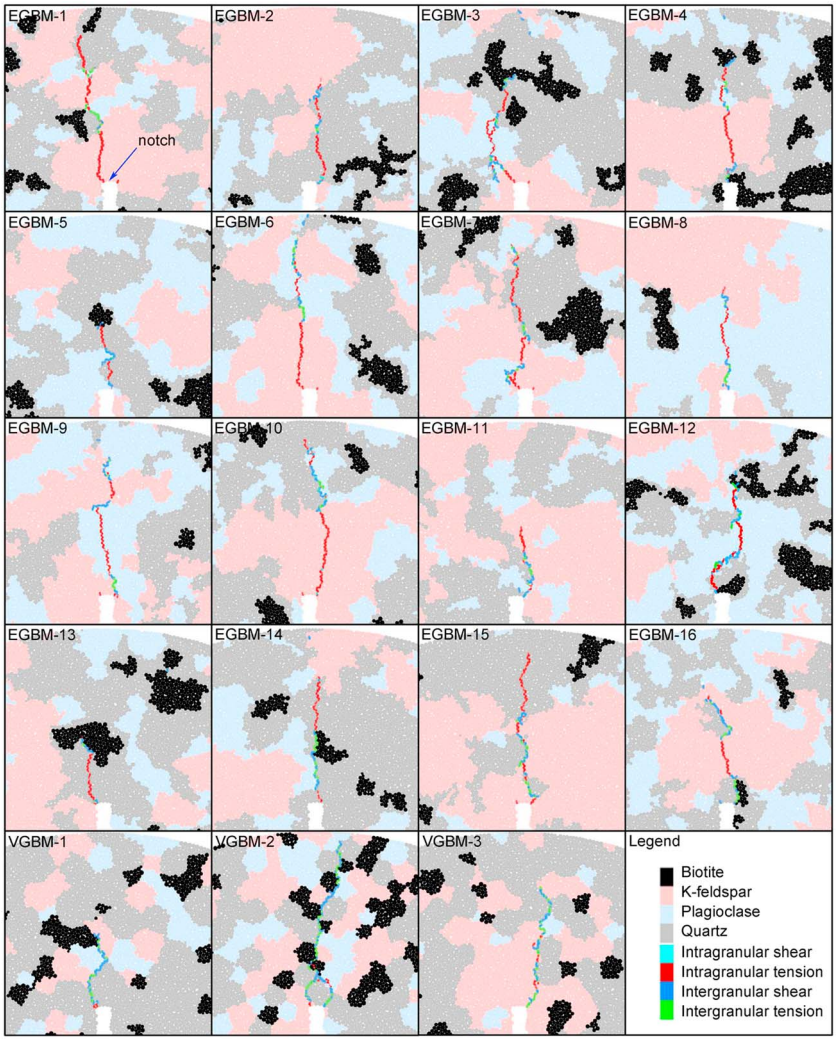

Figure 14. Distributions of four different types of microcracks in 16 extended GBMs and 3 Voronoi GBMs. EGBM-4 is used for model calibration (refer to Figure 12).

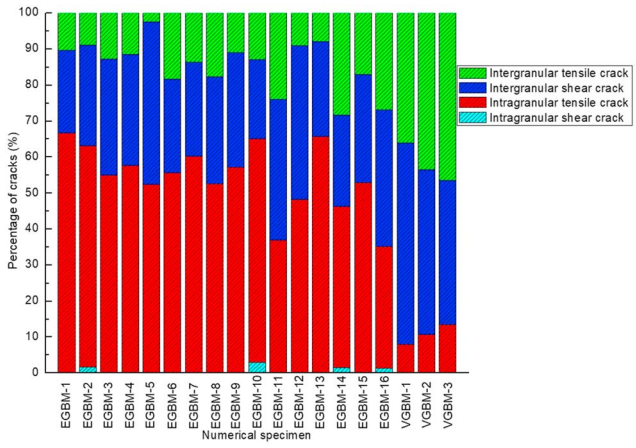

Figure 15. Percentages of the four types of microcracks in 16 extended GBMs and 3 Voronoi GBMs.

with DFN models removed from these numerical models. Figure 19 compares the results with and without DFN models applied.

It seems that the effect of initial microcracks on rock fracturing behavior is not prominent, and the influence is even less on load bearing capacity: only 6.62% and 5.12% increase in peak load in EGBM-5 and EGBM-14 respectively is observed after the removal of DFN, while the remaining 14 EGBMs have almost no changes. It is argued that the main reasons are (1) only the initial microcracks in quartz are considered in this study for simplicity and (2) the weakening factor is high (α_m = 0.8). The first assumption constrains the spatial influence of the DFN model within the considered domain. The second condition, on the other hand, diminishes the influence of the DFN model in terms of degrading mineral strength and inducing stress concentration. However, it by no means implies that the incorporation of initial microcracks has little impact on rock mechanical behavior. Mahabadi et al. (2014) demonstrated that adding microcracks into a rock model caused stress redistribution with higher local tensile stresses and stronger stress gradients.

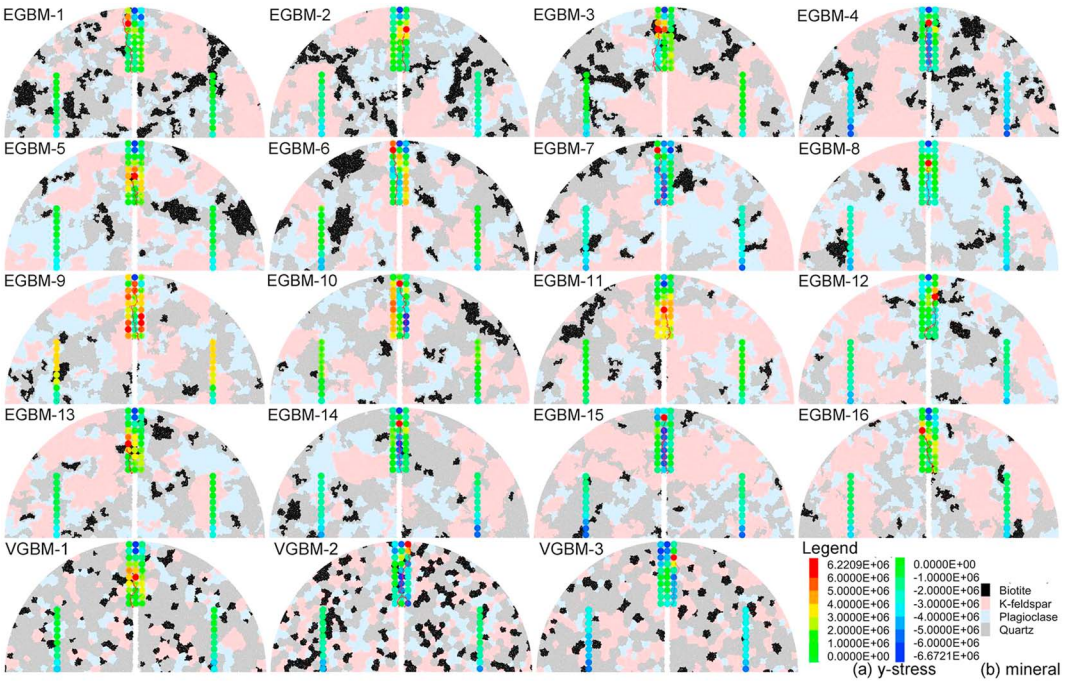

Figure 16. Arrangement of measurement circles showing the distribution of *y* stress (the main crack is shown in red which is the same color of the maximum positive *y* stress for clarity. Compressive stress is negative by convention).

Therefore, it is predictable that if a lower value of α_m (denoting stronger mechanical weakening) is assigned and different DFN models are applied to different minerals, the fracturing behavior and mechanical response of the rock will be noticeably different.

A closer observation of the difference between the cracks before and after removal of DFN models reveals that grain boundary is vulnerable to initial microcracks, because most of the changes to the crack occur along grain interfaces while the intragranular microcracks are barely affected (see Figure 19). These changes are noted by microcrack type and crack shape. For example, in EGBM-1, the dominant failure mode along quartz-plagioclase boundaries changes from tension (green) to shear (blue), indicating that sliding along gain interface as opposed to opening is more promoted in the latter case. In EGBM-2, the main crack tends to deviate from quartz K-feldspar boundaries to quartz grains by uninstallation of DFN. The opposite is noticed in EGBM-14. The main crack shows greater tortuosity by introducing more intergranular microcracks. The above observations point out the deficiency of a purely deterministic GBM in describing micromechanics of rock fracturing, and thus highlighting the consideration of initial microcracks for reliable evaluation.

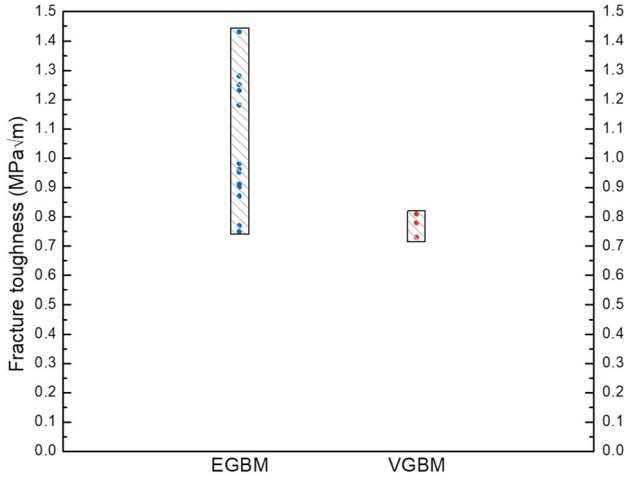

Figure 17. Comparison of fracture toughness of extended GBMs and Voronoi GBMs.

5.4. Classification of Cracking Patterns

In comprehensive consideration of rock microstructures on controlling fracturing behavior and macromechanical properties, the cracking patterns of the 16 EGBMs are classified into four types with respect to the fracture toughness and crack initiation threshold. Fracture toughness of each specimen is normalized by the value of the laboratory specimen (1.279 MPa·m$^{0.5}$), and the crack initiation threshold is defined as the ratio of the stress at which the first microcrack appears to the peak stress. In Figure 20, the normalized fracture toughness and crack initiation threshold of the 16 extended GBMs are plotted versus the cracking pattern. The four cracking patterns with corresponding laboratory observations are presented in Appendix A4.

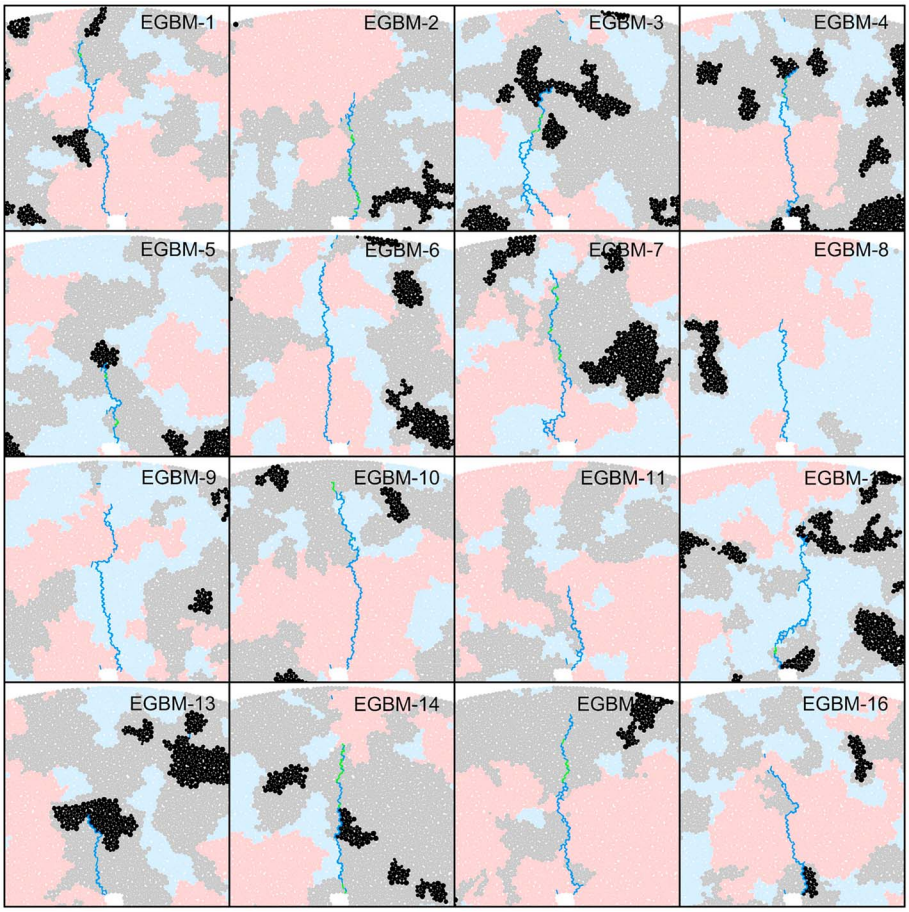

Figure 18. Bicolored microcracks showing the influence of initial microcracks (green lines denote the microcracks coinciding with the installed DFN).

Type 1: High fracture toughness and high crack initiation threshold (EGBM-1, EGBM-6, EGBM-10 in Figure 14). The notch tip is largely occupied by a major grain (K-feldspar). The main fracture initiates from and develops straightforwardly in this region until the grain boundary is encountered, characterized by a smooth, long fracture trajectory. The microcracking behavior is consequentially dominated by the properties of the major grain and less affected by grain boundary properties. Because the onset of crack growth and subsequent crack propagation require to break more intragranular bonds (parallel bonds) that have relatively higher strength, both crack initiation and fracture toughness occur at a high stress level.

Type 2: High fracture toughness and low crack initiation threshold (EGBM-3, EGBM-7, EGBM-9, EGBM-15 in Figure 14). Different mineral grains surround the notch tip, so crack initiation is preferentially localized along grain boundaries, resulting in a low initiation stress. Then, the main crack traverses multiple grain(s). As a special case, EGBM-3 presents two main cracks with more tortuous geometry and has the highest fracture toughness among all the EGBMs. The first microcrack is an intergranular shear crack, which is responsible for the onset of crack growth. In addition, the location of the intergranular microcrack (in blue) indicates that failure does not necessarily start from the tip of the macroscopically visible crack but may be some distance away due to complex arrangement of mineral grains that induce local heterogeneity. Both Type 1 and Type 2 cracks take a long pathway in grains that are related to breakage of more parallel bonds, thus allowing progressive energy dissipation. This plausibly explains why these models have a high fracture toughness.

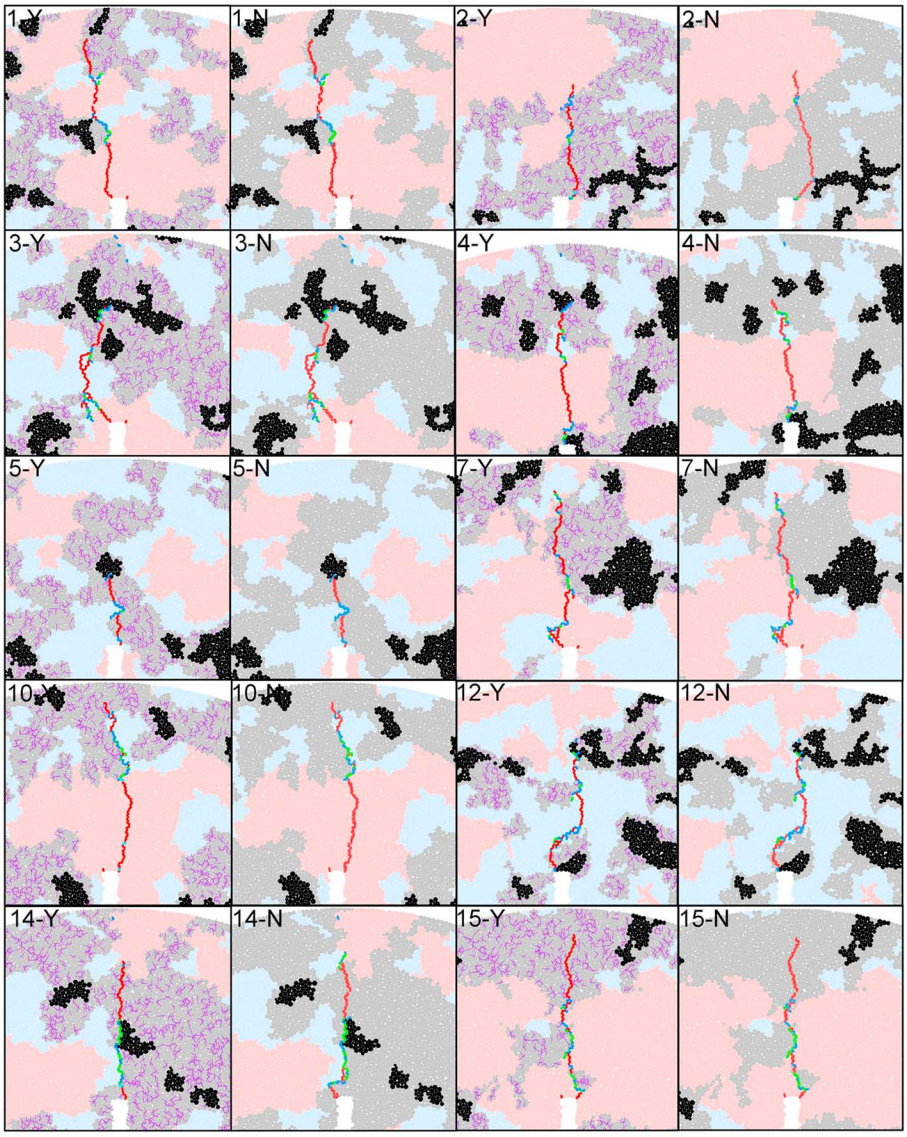

Figure 19. Comparison of the microcracking behavior with and without consideration of initial microcracks. The numerical model is named as *number-Y/N*, where number refers to the number of extended GBM ans Y and N correspond to with and without installation of DFN model, respectively. Weakened bonds in quartz representing initial microcracks are denoted in purple lines. Color representation refers to Figure 14.

Type 3: Low fracture toughness and high crack initiation threshold (EGBM-2, EGBM-12, EGBM-13, and EGBM-14 in Figure 14). Most of the microcracks develop in the quartz region or along grain boundaries because quartz grains occupy a great portion of the cracking area from a microstructural perspective. When comparing Type 1 and Type 3, which are respectively characterized by aggregation of K-feldspar and quartz, specimens of Type 3 have slightly lower fracture toughness than those of Type 1, indicating the contribution of local mineralogical characteristics to fracture toughness. However, this is contradictory to intuitive judgment since the strength of quartz should be higher than that of K-feldspar. One possible reason is that crack propagation along grain boundaries leads to rapid energy dissipation, characterized by a short path of macrofracture (e.g., EGBM-13). On the other hand, development of cracks within quartz grains is not necessarily harder than in K-feldspar with the introduction of a DFN model. It was previously shown that about 30% of intragranular microcracks in quartz coincide with the weakened bonds (in EGBM-2, EGBM-12, and EGBM-14).

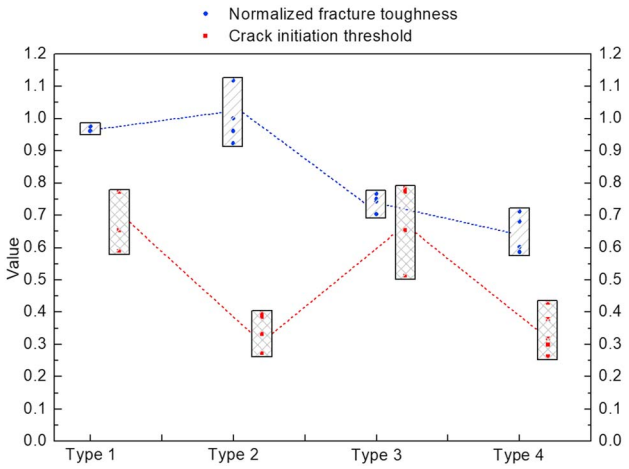

Figure 20. Relationship of cracking pattern with fracture toughness and crack initiation threshold.

Therefore, both microstructural and minerological characteristics contribute to the variation of fracture toughness.

Type 4: Low fracture toughness and low crack initiation threshold (EGBM-4, EGBM-5, EGBM-8, EGBM-11, and EGBM-16 in Figure 14). As with Type 2, the initial cracking point appears at the grain interface, which gives rise to a low crack initiation stress. However, cracks in EGBM-5 and EGBM-11 show a noticeable short and tortuous fracture pathway, because crack propagation within grain boundary channels dissipates most of the energy. In EGBM-4, EGBM-8, and EGBM-16, the main fracture passes through an intact grain and ends up at the interface. Although a long crack trajectory is observed in these EGBMs, they bear low resistance to fracture propagation. We infer that before entering the intact grain, a crack traveling along a grain boundary has intensified the movement of particles of the related grain, which makes breakage of intragranular bonds much easier. Hence, fracture length is not necessarily positively related to fracture toughness.

6. Discussion

6.1. Semicircular Bending Test

In brittle fracture mechanics, fracture toughness is a crucial indicator of the ability to resist crack propagation, which is used as a criterion for predicting fracture initiation (Nasseri & Mohanty, 2008; Wei et al., 2017). Semicircular bending test is one of the four suggested methods for the determination of Mode I fracture toughness (International Society for Rock Mechanics, 2007). Compared with the other methods, that is, chevron bend specimen, short rod specimen, semicircular bend specimen, and cracked chevron notched Brazilian disk specimen, the advantages of semicircular bending test are (1) long intact rock cores are not required for specimen preparation and (2) the testing apparatus is relatively simple (Chang et al., 2002; Cui et al., 2010). By simulating semicircular bending test, we are able to directly evaluate the fracability of the material.

Another reason for taking Mode I fracture toughness into calibration is to match the tensile strength, given the strong linear correlation between tensile strength and Mode I fracture toughness (Hanson et al., 1994):

$$\sigma_t = \alpha_0 K_{IC} \tag{6}$$

where σ_t and K_{IC} are the tensile strength and Mode I fracture toughness of rock and $\alpha_0$is a constant depending on the rock type.

It is noteworthy that the maximum compressive load (P_{max}) of the calibrated numerical model is 66.3 kN, which is about 22 times higher than the real laboratory data (in Figure 12). This discrepancy is mostly attributed to the mismatch of the geometric parameters between a 2-D model and the 3-D physical specimen involved in equation (4), especially the thickness (the thickness of a PFC2D model is 1 meter by default). It indicates that if the Mode I fracture toughness (tensile strength) is well calibrated by simulating semicircular bending test, the maximum loading force has to be much higher as compared to the real value. The assumption involved in the 2-D scenario may be an inherent source of unreliability of the simulation results. These topics should be addressed in future studies by developing a 3-D model.

6.2. Limitations of GBM

1. Grain-based modeling approach is particularly suitable for simulating highly interlocked, low-porosity materials. For some other porous or clastic sedimentary rocks (sandstone, shale, etc.), GBM is rarely applicable. Without modification, the microstructural defects cannot be incorporated into the model. This is one of the major motivations of improving GBM by introducing a DFN model to account for the effect of initial microcracks. Although GBM is more capable of reproducing the mineralogical and geometrical heterogeneity of rocks as compared with the bonded particle model, one implication in

the modeling is that each mineral is isotropic. In the real situation, minerals are all anisotropic presented by crystalline substances. It remains difficult to take the structure of minerals into account by current numerical techniques.

2. Despite the considerable work in calibration of a GBM, there is no universally accepted method for determining a unique set of microparameters, owing to the complicated interplay of multiple microparameters associated with mineralogy and microstructural heterogeneity in controlling the macroscopic behavior of the material. The calibration process has to be somehow subjective based on an understanding of physical meanings of the microparameters, as well as personal experience. Even if the model shows the expected behavior in the mechanical tests, how each parameter is truly assigned has not been addressed. Specifically, we first propose to integrate a DFN model into GBM to simulate the presence of initial microcracks whereby the parallel bonds are weakened. The parallel bond strength weakening factor, α_m, is determined by the authors. Owing to the fact that the granite sample we modeled in this study is intact and fresh, the microcracks observed in the thin section are almost closed. Therefore, the weakening factor is assigned with a high value. If a weathered rock in which open microcrack are widely distributed is modeled, a weakening factor of around 0 indicating no or almost no tensile strength and cohesion would be more realistic. Partially due to an overestimated value of α_m (= 0.8), the effect of initial microcracks on microcracking behavior is less significant than expected. Reliable calibration of α_m may be further investigated by understanding of microcracks on the strength weakening of each mineral.

7. Conclusions

Reliable prediction of rock fracturing by means of numerical simulation highly depends on the confidence of the modeled rock structure. The GBM approach has been proved to be particularly suitable for modeling the rock failure process. However, in previous Voronoi GBM simulations, grain structure is statistically reproduced, which overlooks the uniqueness of microstructures. Besides, other preexisting (intragranular and intergranular) microcracks attributed to weathering, cleavage, etc., are not explicitly considered in GBM. Focusing on the microstructual heterogeneity contributed by grain boundary and initial microcracks, an extended grain-based model is proposed by integrating GBM in the particle flow code and a DFN model to interpret the behavior of rock fracturing subjected to external loadings. Compared with Voronoi GBM, the proposed extended GBM is characterized by (1) deterministic mapping of microstructures by the use of digital image processing and (2) incorporation of the effect of initial microcracks via applying a DFN model.

Sixteen extended GBMs and three Voronoi GBMs are examined by semicircular bending tests. Model calibration is performed through matching the simulation results with the laboratory observations regarding the macromechanical properties and macrocracking pattern. Since the models are shaped in the same geometry and dimension and tested under the same condition, great variations of the macrofracture pattern clearly indicates the deterministic role of microstructures in rock fracturing. Hence, a Voronoi GBM or a purely deterministic GBM is insufficient in interpreting fracturing mechanisms.

In terms of microcracking characteristics, the orientation of microcracks shows a significant dependence on its mode: intragranular microcracks preferably align parallel or subparallel to the loading direction, whereas intergranular microcracks are randomly oriented depending on the orientation of grain boundaries. As a result, the crack path within grains is smoother than along grain boundaries. Intragranular microcracks dominate in extended GBM, while failure of Voronoi GBM is primarily attributed to intergranular cracking. The percentages of intergranular cracks in the extended GBM and the statistical Voronoi GBM suggest that Voronoi GBM overestimates the role of intergranular cracks in controlling rock cracking due to the underestimation of grain clustering. Because failure of smooth joint contact is easier than that of parallel bond, statistical description of grain structure will result in a lower fracture toughness and a zigzag macrofracture path due to the random arrangement of grains.

By removal of DFN from the extended GBM, we find that most of the changes including microcrack type and macrocrack shape appear at grain interfaces, which indicates that cracking behavior along grain boundaries is more vulnerable to initial microcracks. Compared with the decisive role of rock fabric, the effect of DFN seems to be limited, especially for those with no/little quartz grains occupying the fracture zone.

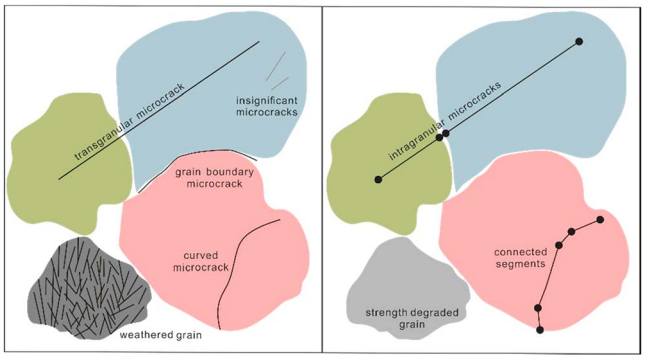

Figure A1. Conceptualization of principles of microcrack analysis: the real situation of microcracks observed in thin section (left) and simplifications adopted in collection of microcrack statistics (right).

Nevertheless, this is probably due to a high weakening factor assigned to degrade the parallel bond strength and the assumption that only the initial microcracks within quartz are considered.

To generalize the impact of the microstructural characteristics on macroscopic properties, it is the first time cracking patterns are classified into four types with respect to fracture toughness and crack initiation threshold. Crack initiation level is controlled by microcracking mode: failure starting from grain boundary leads to a low initiation stress, while onset of crack within the mineral gives rise to a high value. The first microcrack may not appear exactly at the notch tip, but at a distance away depending on the local microsctructures. Higher fracture toughness is generally characterized by a smooth, long pathway that allows progressive energy dissipation, but not vice versa owing to the complex micromechanisms involved in the cracking behavior. First, intergranular cracking noted by a tortuous and poorly developed crack track provides a rapid way for energy attenuation. Second, cracking along grain boundaries may also intensify the movement of particles that makes intragranular bonds more vulnerable to break. Third, the presence of initial microcracks can lower the ability of the rock to resist crack propagation within grains. Although fractures probably develop well in the latter two cases, fracture toughness tends to be lower than expected.

Appendix A

A1. Principles of Microcrack Analysis

1. Each microcrack is regarded as a straight line, while curved microcracks are recorded as multiple connected straight traversing segments or a straight line that can show their overall orientation and length.

Table A1
Calibrated Microparameters for Kowloon Granite

		Parameters for minerals			
Microparameter	Symbol (unit)	Quartz	K-feldspar	Plagioclase	Biotite
Minimum particle radius	R_{min} (mm)	0.09	0.09	0.09	0.09
Particle size ratio	R_{max}/R_{min}	2.0	2.0	2.0	2.0
Particle density *	ρ (kg/m^3)	2650	2600	2600	2850
Particle friction coefficient *	μ	1.2	1.2	1.2	1.2
Contact normal to shear stiffness ratio #~	k_n/k_s	1.0	1.6	1.7	1.1
Particle-particle contact modulus #~	E_c (GPa)	64	40	52	24
Parallel bond radius multiplier *	λ	1	1	1	1
Parallel bond normal to shear stiffness ratio #~	k_n/k_s	1.0	1.6	1.7	1.1
Parallel bond modulus #~	E_c (GPa)	64	40	52	24
Parallel bond tensile strength #	σ_c (MPa)	39.1	37.6	37.6	36.0
Parallel bond cohesion #	$\bar{C}$ (MPa)	39.1	37.6	37.6	36.0
Parallel bond friction angle #	φ (deg)	30	30	30	30
Parallel bond strength weakening factor	α_m	0.8	—	—	—
		Parameters for mineral boundaries (smooth joint)			
Smooth-joint normal stiffness factor *	α	0.6			
Smooth-joint shear stiffness factor #	α	0.8			
Smooth-joint bond tensile strength ~	σ_c (MPa)	14			
Smooth-joint bond cohesion #~	C (MPa)	13			
Smooth-joint bond friction angle #	ϕ (deg)	30			
Smooth-joint bond friction coefficient *	μ	1.2			

Note. The microparameters are mainly retrieved from the literature (Hofmann, Babadagli, Zimmermann, 2015). No changes are made to those marked by the symbol *. Major adjustment is made to the microparameters with the mark # when calibrating to uniaxial compressive strength, Young's modulus and Mode I fracture toughness. Minor adjustment is made to the microparameters with the mark ~ when matching the cracking pattern in the semicircular bending test. The remaining microparameters without mark are decided by the authors.

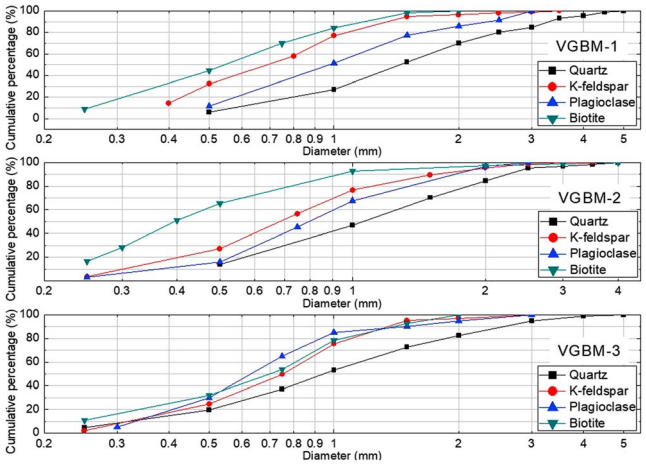

Figure A2. Grain size distributions of different minerals.

2. Grain boundary cracks are excluded, since very few open grain boundaries are observed in the thin section. The mechanical impact of grain boundaries on the numerical specimen is accounted by smooth joint contacts via installation of grain boundary fabric.
3. Only significant microcracks are recorded. The definition of *insignificant* as opposed to *significant* depends on the comparison of the microcrack length and the grain size. If the microcrack length is estimated to be one order smaller than the grain, it is accounted as an insignificant microcrack.
4. Cracks across multiple mineral grains (transgranular microcracks) are split at the grain boundaries and treated as individual segments (intragranular microcracks).
5. Microcracks in a zone of excessively high density of microcracks attributed to severe local weathering are excluded, the effect of which is accounted by degraded parallel bond properties.

The aforementioned principles are also graphically illustrated in Figure A1.

A2. Calibrated Microparameters of GBM

All the calibrated microparameters in the present study are listed in Table A1.

A3. Input Parameters for Generation of Voronoi Tessellations

Mineral compositions and grain size distribution of each mineral are the two input parameters to generate a Voronoi tessellation. Thin section is therefore analyzed with the assistance of the computer program ImageJ (https://imagej.net/Welcome) for data acquisition. The mineral grain size is measured by the equivalent diameter (*De*), which is defined as the diameter of a circle with an equal area of the grain in cross section:

$$De = \sqrt{4A/\pi} \tag{A1}$$

where A is the area of a circled mineral grain.

Mineral composition is calculated by the sum of the area of a mineral (A) over the sum of the area of all the minerals observed in the thin section:

$$\text{Mineral Composition} = \frac{\sum \text{Area of Mineral } A}{\sum \text{Area of all Minerals}} \tag{A2}$$

Figure A2 and Table A2 present the results of analysis of three thin sections from different rock specimens.

Table A2
Mineral Contents of Different VGBMs

Numerical model	Mineral content (%)			
	Quartz	K-feldspar	Plagioclase	Biotite
VGBM-1	64.75	18.17	11.54	5.54
VGBM-2	37.38	26.03	20.65	15.94
VGBM-3	59.02	27.91	6.12	6.95

A4. Four types of Cracking Patterns

Four types of cracking patterns are generalized from the numerical results with respect to fracture toughness and crack initiation threshold. Each pattern is well observed in laboratory tests, which are compared as follows (Figure A3):

1. Type 1: High fracture toughness and high crack initiation threshold.
2. Type 2: High fracture toughness and low crack initiation threshold.
3. Type 3: Low fracture toughness and high crack initiation threshold.
4. Type 4: Low fracture toughness and low crack initiation threshold.

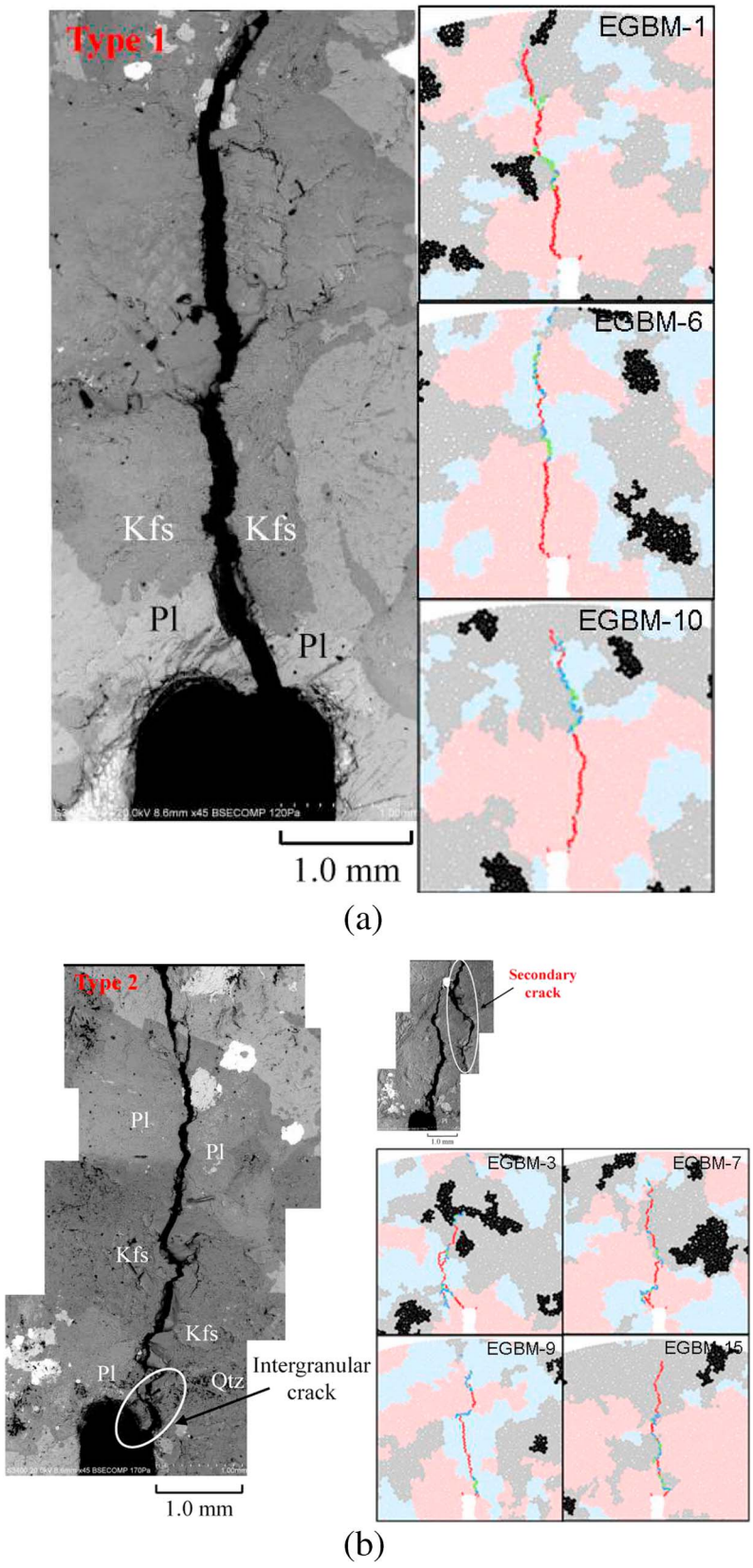

Figure A3. Four types of cracking patterns observed in numerical simulations and laboratory tests.

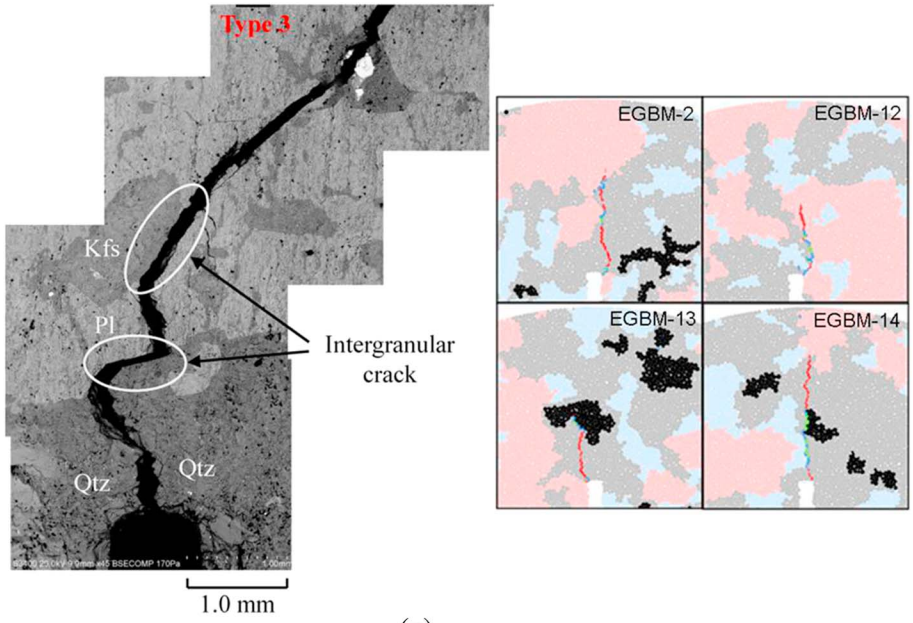

(c)

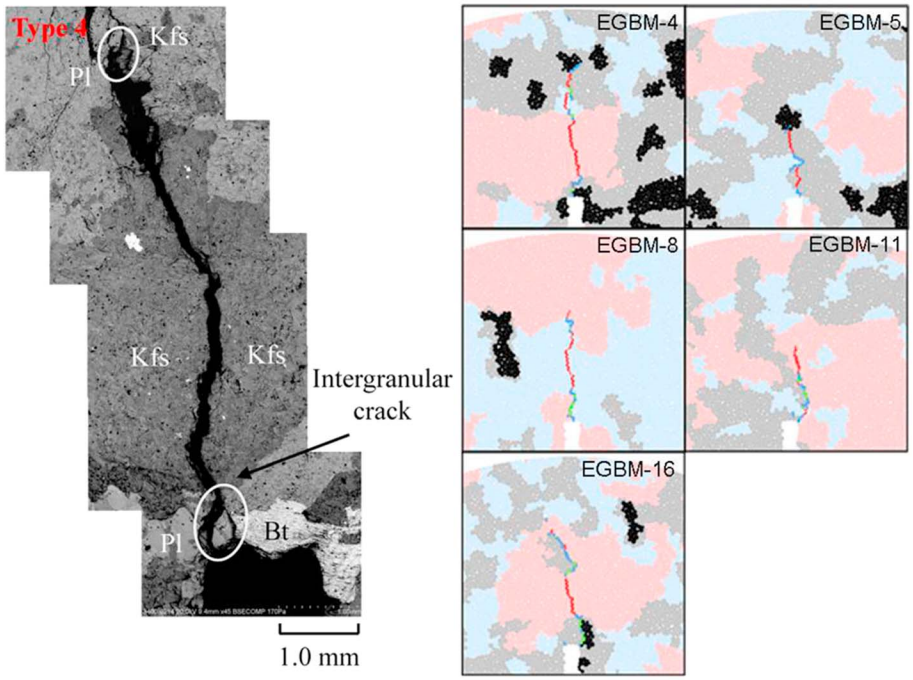

(d)

Figure A3. (continued)

Acknowledgments
The authors acknowledge the support from the National Science Foundation of China (grant 41877217), the Startup fund, Seed Funding Programme for Basic Research for New Staff at the University of Hong Kong, the General Research Fund (17303917) of the Research Grants Council (Hong Kong), the Hung Hing Ying Physical Sciences Research Fund 2017-18, and the HKU SPACE Research Fund. The first author acknowledges the Postgraduate Scholarship from the University of Hong Kong. The authors would also like to thank Tianyang Guo and Jay Ng for their supportive work in sampling and analysis of thin sections. The data used for numerical analysis in this study can be accessed in Appendix A.

References

Bahrani, N., Kaiser, P. K., & Valley, B. (2014). Distinct element method simulation of an analogue for a highly interlocked, non-persistently jointed rockmass. *International Journal of Rock Mechanics and Mining Sciences*, *71*, 117–130. https://doi.org/10.1016/j.ijrmms.2014.07.005

Brideau, M. A., Yan, M., & Stead, D. (2009). The role of tectonic damage and brittle rock fracture in the development of large rock slope failures. *Geomorphology*, *103*(1), 30–49. https://doi.org/10.1016/j.geomorph.2008.04.010

Cai, M. (2013). Fracture initiation and propagation in a Brazilian disc with a plane interface: A numerical study. *Rock Mechanics and Rock Engineering*, *46*(2), 289–302. https://doi.org/10.1007/s00603-012-0331-1

Cai, M., & Horii, H. (1992). A constitutive model of highly jointed rock masses. *Mechanics of Materials*, *13*(3), 217–246. https://doi.org/10.1016/0167-6636(92)90004-W

Chang, S. H., Lee, C. I., & Jeon, S. (2002). Measurement of rock fracture toughness under modes I and II and mixed-mode conditions by using disc-type specimens. *Engineering Geology*, *66*(1–2), 79–97. https://doi.org/10.1016/S0013-7952(02)00033-9

Chen, Q., Nezhad, M. M., Fisher, Q., & Zhu, H. H. (2016). Multi-scale approach for modeling the transversely isotropic elastic properties of shale considering multi-inclusions and interfacial transition zone. *International Journal of Rock Mechanics and Mining Sciences*, *84*, 95–104. https://doi.org/10.1016/j.ijrmms.2016.02.007

Chen, S., Yue, Z. Q., & Tham, L. G. (2004). Digital image-based numerical modeling method for prediction of inhomogeneous rock failure. *International Journal of Rock Mechanics and Mining Sciences*, *41*(6), 939–957. https://doi.org/10.1016/j.ijrmms.2004.03.002

Cheng, Y., Wong, L. N. Y., & Zou, C. (2015). Experimental study on the formation of faults from en-echelon fractures in Carrara marble. *Engineering Geology*, *195*, 312–326. https://doi.org/10.1016/j.enggeo.2015.06.004

Cho, N. A., Martin, C. D., & Sego, D. C. (2007). A clumped particle model for rock. *International Journal of Rock Mechanics and Mining Sciences*, *44*(7), 997–1010. https://doi.org/10.1016/j.ijrmms.2007.02.002

Cui, Z. D., Liu, D. A., An, G. M., Sun, B., Zhou, M., & Cao, F. Q. (2010). A comparison of two ISRM suggested chevron notched specimens for testing mode-I rock fracture toughness. *International Journal of Rock Mechanics and Mining Sciences*, *47*(5), 871–876. https://doi.org/10.1016/j.ijrmms.2009.12.015

Dershowitz, W. S., & Einstein, H. H. (1988). Characterizing rock joint geometry with joint system models. *Rock Mechanics and Rock Engineering*, *21*(1), 21–51. https://doi.org/10.1007/BF01019674

Dokhani, V., Yu, M., & Bloys, B. (2016). A wellbore stability model for shale formations: Accounting for strength anisotropy and fluid induced instability. *Journal of Natural Gas Science and Engineering*, *32*, 174–184. https://doi.org/10.1016/j.jngse.2016.04.038

Duan, K., & Kwok, C. Y. (2015). Discrete element modeling of anisotropic rock under Brazilian test conditions. *International Journal of Rock Mechanics and Mining Sciences*, *78*, 46–56. https://doi.org/10.1016/j.ijrmms.2015.04.023

Feng, X. T., Ding, W., & Zhang, D. (2009). Multi-crack interaction in limestone subject to stress and flow of chemical solutions. *International Journal of Rock Mechanics and Mining Sciences*, *46*(1), 159–171. https://doi.org/10.1016/j.ijrmms.2008.08.001

Gandossi, L. (2013). An overview of hydraulic fracturing and other formation stimulation technologies for shale gas production. Eur. Commisison Jt. Res. Cent. Tech. Reports. https://doi.org/10.2790/99937

Gonzalez, R. C., & Woods, R. E. (2012). Digital image processing.

Hajiabdolmajid, V., & Kaiser, P. (2003). Brittleness of rock and stability assessment in hard rock tunneling. *Tunnelling and Underground Space Technology*, *18*(1), 35–48. https://doi.org/10.1016/S0886-7798(02)00100-1

Hamdi, P., Stead, D., & Elmo, D. (2015). Characterizing the influence of stress-induced microcracks on the laboratory strength and fracture development in brittle rocks using a finite-discrete element method-micro discrete fracture network FDEM-μDFN approach. *Journal of Rock Mechanics and Geotechnical Engineering*, *7*(6), 609–625. https://doi.org/10.1016/j.jrmge.2015.07.005

Hanson, J. A., Hardin, B. O., & Mahboub, K. (1994). Fracture toughness of compacted cohesive soils using ring test. *Journal of Geotechnical EngineeringJournal of Geotechnical Engineering*, *120*(5), 872–891. https://doi.org/10.1061/(ASCE)0733-9410(1994)120:5(872)

Hazzard, J. F., Young, R. P., & Maxwell, S. C. (2000). Micromechanical modeling of cracking and failure in brittle rocks. *Journal of Geophysical Research*, *105*, 16,683–16,697. https://doi.org/10.1029/2000JB900085

He, J., & Afolagboye, L. O. (2017). Influence of layer orientation and interlayer bonding force on the mechanical behavior of shale under Brazilian test conditions. *Acta Mechanica Sinica*, 1–10. https://doi.org/10.1007/s10409-017-0666-7

Hofmann, H., Babadagli, T., Yoon, J. S., Zang, A., & Zimmermann, G. (2015). A grain based modeling study of mineralogical factors affecting strength, elastic behavior and micro fracture development during compression tests in granites. *Engineering Fracture Mechanics*, *147*, 261–275. https://doi.org/10.1016/j.engfracmech.2015.09.008

Hofmann, H., Babadagli, T., & Zimmermann, G. (2015). A grain based modeling study of fracture branching during compression tests in granites. *International Journal of Rock Mechanics and Mining Sciences*, *77*, 152–162. https://doi.org/10.1016/j.ijrmms.2015.04.008

International Society for Rock Mechanics. (2007). The complete ISRM suggested methods for rock characterization, testing and monitoring: 1974–2006. International Soc. for Rock Mechanics, Commission on Testing Methods.

Kuruppu, M. D., Obara, Y., Ayatollahi, M. R., Chong, K. P., & Funatsu, T. (2014). ISRM-suggested method for determining the mode I static fracture toughness using semi-circular bend specimen. *Rock Mechanics and Rock Engineering*, *47*(1), 267–274. https://doi.org/10.1007/s00603-013-0422-7

Lajtai, E. Z. (1998). Microscopic fracture processes in a granite. *Rock Mechanics and Rock Engineering*, *31*(4), 237–250. https://doi.org/10.1007/s006030050023

Lewis, A. C., & Geltmacher, A. B. (2006). Image-based modeling of the response of experimental 3D microstructures to mechanical loading. *Scripta Materialia*, *55*(1), 81–85. https://doi.org/10.1016/j.scriptamat.2006.01.043

Li, J., Konietzky, H., & Frühwirt, T. (2017). Voronoi-based DEM simulation approach for sandstone considering grain structure and pore size. *Rock Mechanics and Rock Engineering*, *50*(10), 2749–2761. https://doi.org/10.1007/s00603-017-1257-4

Li, Z., Wong, L. N. Y., & Teh, C. I. (2017). Low cost colorimetry for assessment of fire damage in rock. *Engineering Geology*, *228*, 50–60. https://doi.org/10.1016/j.enggeo.2017.07.006

Lim, S. S., Martin, C. D., & Åkesson, U. (2012). In-situ stress and microcracking in granite cores with depth. *Engineering Geology*, *147*, 1–13. https://doi.org/10.1016/j.enggeo.2012.07.006

Lisjak, A., Grasselli, G., & Vietor, T. (2014). Continuum–discontinuum analysis of failure mechanisms around unsupported circular excavations in anisotropic clay shales. *International Journal of Rock Mechanics and Mining Sciences*, *65*, 96–115. https://doi.org/10.1016/j.ijrmms.2013.10.006

Lisjak, A., Tatone, B. S., Grasselli, G., & Vietor, T. (2014). Numerical modelling of the anisotropic mechanical behaviour of opalinus clay at the laboratory-scale using FEM/DEM. *Rock Mechanics and Rock Engineering*, *47*(1), 187–206. https://doi.org/10.1007/s00603-012-0354-7

Liu, G., Cai, M., & Huang, M. (2018). Mechanical properties of brittle rock governed by micro-geometric heterogeneity. *Computers and Geotechnics*. https://doi.org/10.1016/j.compgeo.2017.11.013

Liu, H. Y., Kou, S. Q., Lindqvist, P. A., & Tang, C. A. (2007). Numerical modelling of the heterogeneous rock fracture process using various test techniques. *Rock Mechanics and Rock Engineering*, *40*(2), 107–144. https://doi.org/10.1007/s00603-006-0091-x

Mahabadi, O. K. (2012). Investigating the influence of micro-scale heterogeneity and microstructure on the failure and mechanical behaviour of geomaterials (Doctoral dissertation, University of Toronto (Canada)).

Mahabadi, O. K., Tatone, B. S. A., & Grasselli, G. (2014). Influence of microscale heterogeneity and microstructure on the tensile behavior of crystalline rocks. *Journal of Geophysical Research: Solid Earth*, *119*, 5324–5341. https://doi.org/10.1002/2014JB011064

Mark, R., & Billo, E. (2002). Application of digital image enhancement in rock art recording. *American Indian Rock Art*, *28*, 121–128.
McClure, M. W., & Horne, R. N. (2014). An investigation of stimulation mechanisms in enhanced geothermal systems. *International Journal of Rock Mechanics and Mining Sciences*, *72*, 242–260. https://doi.org/10.1016/j.ijrmms.2014.07.011
Meng, Z., & Pan, J. (2007). Correlation between petrographic characteristics and failure duration in clastic rocks. *Engineering Geology*, *89*(3–4), 258–265. https://doi.org/10.1016/j.enggeo.2006.10.010
Morgan, S. P., & Einstein, H. H. (2017). Cracking processes affected by bedding planes in Opalinus shale with flaw pairs. *Engineering Fracture Mechanics*, *176*, 213–234. https://doi.org/10.1016/j.engfracmech.2017.03.003
Morgan, S. P., Johnson, C. A., & Einstein, H. H. (2013). Cracking processes in Barre granite: Fracture process zones and crack coalescence. *International Journal of Fracture*, *180*(2), 177–204. https://doi.org/10.1007/s10704-013-9810-y
Nasseri, M. H. B., & Mohanty, B. (2008). Fracture toughness anisotropy in granitic rocks. *International Journal of Rock Mechanics and Mining Sciences*, *45*(2), 167–193. https://doi.org/10.1016/j.ijrmms.2007.04.005
Nezhad, M. M., Fisher, Q. J., Gironacci, E., & Rezania, M. (2018). Experimental study and numerical modeling of fracture propagation in shale rocks during Brazilian disk test. *Rock Mechanics and Rock Engineering*, 1–21. https://doi.org/10.1007/s00603-018-1429-x
Nezhad, M. M., Zhu, H., Woody Ju, J., & Chen, Q. (2016). A simplified multiscale damage model for the transversely isotropic shale rocks under tensile loading. *International Journal of Damage Mechanics*, *25*(5), 705–726. https://doi.org/10.1177/1056789516639531
Park, B., & Min, K. B. (2015). Bonded-particle discrete element modeling of mechanical behavior of transversely isotropic rock. *International Journal of Rock Mechanics and Mining Sciences*, *76*, 243–255. https://doi.org/10.1016/j.ijrmms.2015.03.014
Peng, J., Wong, L. N. Y., & Teh, C. I. (2017). Influence of grain size heterogeneity on strength and microcracking behavior of crystalline rocks. *Journal of Geophysical Research: Solid Earth*, *122*, 1054–1073. https://doi.org/10.1002/2016JB013469
Plataniotis, K. N., & Venetsanopoulos, A. N. (2013). *Color image processing and applications*. Berlin, Germany: Springer Science & Business Media.
Potyondy, D. O. (2010). A grain-based model for rock: approaching the true microstructure. Proceedings of rock mechanics in the Nordic Countries, 9–12.
Potyondy, D. O., & Cundall, P. A. (2004). A bonded-particle model for rock. *International Journal of Rock Mechanics and Mining Sciences*, *41*(8), 1329–1364. https://doi.org/10.1016/j.ijrmms.2004.09.011
Prange, M. D., & LeFranc, M. (2018). Characterizing fracture geometry from borehole images. *Mathematical Geosciences*, 1–30. https://doi.org/10.1007/s11004-018-9735-0
Priest, S. D., & Hudson, J. A. (1981, June). Estimation of discontinuity spacing and trace length using scanline surveys. *International Journal of Rock Mechanics and Mining Science and Geomechanics Abstracts*, *18*(3), 183–197. https://doi.org/10.1016/0148-9062(81)90973-6
Quey, R., Dawson, P. R., & Barbe, F. (2011). Large-scale 3D random polycrystals for the finite element method: Generation, meshing and remeshing. *Computer Methods in Applied Mechanics and Engineering*, *200*(17–-20), 1729–1745. https://doi.org/10.1016/j.cma.2011.01.002
Sedgewick, J. (2002). Differences between a drawing program (Vector Graphics) and a paint program (Image Files). Quick Photoshop for Research: A Guide to Digital Imaging for Photoshop 4x, 5x, 6x, 7x, 17–18.
Selinger, P. (2003). Potrace: A polygon-based tracing algorithm. Potrace (online), http://potrace. sourceforge. net/potrace. pdf (2009-07-01).
Tan, X., Konietzky, H., Frühwirt, T., & Dan, D. Q. (2015). Brazilian tests on transversely isotropic rocks: Laboratory testing and numerical simulations. *Rock Mechanics and Rock Engineering*, *48*(4), 1341–1351. https://doi.org/10.1007/s00603-014-0629-2
Tang, C. A., Liu, H., Lee, P. K. K., Tsui, Y., & Tham, L. (2000). Numerical studies of the influence of microstructure on rock failure in uniaxial compression—Part I: Effect of heterogeneity. *International Journal of Rock Mechanics and Mining Sciences*, *37*(4), 555–569. https://doi.org/10.1016/S1365-1609(99)00121-5
Tkalcic, M., & Tasic, J. F. (2003). Colour spaces: Perceptual, historical and applicational background. *Proceedings of EUROCON*, *1*, 304–308. https://doi.org/10.1109/EURCON.2003.1248032
Tsang, C. F., Bernier, F., & Davies, C. (2005). Geohydromechanical processes in the Excavation Damaged Zone in crystalline rock, rock salt, and indurated and plastic clays -in the context of radioactive waste disposal. *International Journal of Rock Mechanics and Mining Sciences*, *42*(1), 109–125.
Wei, M. D., Dai, F., Xu, N. W., Zhao, T., & Liu, Y. (2017). An experimental and theoretical assessment of semi-circular bend specimens with chevron and straight-through notches for mode I fracture toughness testing of rocks. *International Journal of Rock Mechanics and Mining Sciences*, *99*, 28–38.
Wong, L. N. Y., & Einstein, H. H. (2009a). Crack coalescence in molded gypsum and Carrara marble: Part 1. Macroscopic observations and interpretation. *Rock Mechanics and Rock Engineering*, *9942*(3), 475–511. https://doi.org/10.1016/j.ijrmms.2017.09.004
Wong, L. N. Y., & Einstein, H. H. (2009b). Crack coalescence in molded gypsum and Carrara marble: Part 2—microscopic observations and interpretation. *Rock Mechanics and Rock Engineering*, *42*(3), 475–511. https://doi.org/10.1007/s00603-008-0002-4
Wong, L. N. Y., & Einstein, H. H. (2009c). Systematic evaluation of cracking behavior in specimens containing single flaws under uniaxial compression. *International Journal of Rock Mechanics and Mining Sciences*, *4246*(32), 239–249. https://doi.org/10.1007/s00603-008-0003-3
Xu, C., & Dowd, P. (2010). A new computer code for discrete fracture network modelling. *Computers & Geosciences*, *36*(3), 292–301. https://doi.org/10.1016/j.cageo.2009.05.012
Xu, G., He, C., Chen, Z., & Su, A. (2018). Transverse isotropy of Phyllite under Brazilian tests: Laboratory testing and numerical simulations. *Rock Mechanics and Rock Engineering*, *51*(4), 1111–1135. https://doi.org/10.1007/s00603-017-1393-x
Yang, S. Q., & Huang, Y. H. (2014). Particle flow study on strength and meso-mechanism of Brazilian splitting test for jointed rock mass. *Acta Mechanica Sinica*, *30*(4), 547–558. https://doi.org/10.1007/s10409-014-0076-z
Yang, S. Q., Liu, X. R., & Jing, H. W. (2013). Experimental investigation on fracture coalescence behavior of red sandstone containing two unparallel fissures under uniaxial compression. *International Journal of Rock Mechanics and Mining Sciences*, *63*, 82–92. https://doi.org/10.1016/j.ijrmms.2013.06.008
Yoon, J. (2007). Application of experimental design and optimization to PFC model calibration in uniaxial compression simulation. *International Journal of Rock Mechanics and Mining Sciences*, *44*(6), 871–889. https://doi.org/10.1016/j.ijrmms.2007.01.004
Zang, A., Wagner, F. C., Stanchits, S., Janssen, C., & Dresen, G. (2000). Fracture process zone in granite. *Journal of Geophysical Research*, *105*, 23,651–23,661. https://doi.org/10.1029/2000JB900239
Zeng, X., & Wei, Y. (2017). Crack deflection in brittle media with heterogeneous interfaces and its application in shale fracking. *Journal of the Mechanics and Physics of Solids*, *101*, 235–249. https://doi.org/10.1016/j.jmps.2016.12.012
Zhang, X. P., & Wong, L. N. Y. (2014). Displacement field analysis for cracking processes in bonded-particle model. *Bulletin of Engineering Geology and the Environment*, *73*(1), 13–21. https://doi.org/10.1007/s10064-013-0496-1

Zhang, Y., & Wong, L. N. Y. (2018). A review of numerical techniques approaching microstructures of crystalline rocks. *Computers & Geosciences*, *115*, 167–187. https://doi.org/10.1016/j.cageo.2018.03.012

Zhao, Y., Zhang, L., Wang, W., Pu, C., Wan, W., & Tang, J. (2016). Cracking and stress–strain behavior of rock-like material containing two flaws under uniaxial compression. *Rock Mechanics and Rock Engineering*, *49*(7), 2665–2687. https://doi.org/10.1007/s00603-016-0932-1

Zou, C., & Wong, L. N. Y. (2014). Experimental studies on cracking processes and failure in marble under dynamic loading. *Engineering Geology*, *173*, 19–31. https://doi.org/10.1016/j.enggeo.2014.02.003

Zou, C., Wong, L. N. Y., Loo, J. J., & Gan, B. S. (2016). Different mechanical and cracking behaviors of single-flawed brittle gypsum specimens under dynamic and quasi-static loadings. *Engineering Geology*, *201*, 71–84. https://doi.org/10.1016/j.enggeo.2015.12.014